



NAVAL POSTGRADUATE SCHOOL

MONTEREY, CALIFORNIA

THESIS

**VARIABLE RESOLUTION DIRECTION FINDING USING
THE ROBUST SYMMETRICAL NUMBER SYSTEM**

by

Anthony Lee

December 2006

Thesis Advisors:

Phillip Pace
David Jenn
Donald Walters

Approved for public release; distribution is unlimited

THIS PAGE INTENTIONALLY LEFT BLANK

REPORT DOCUMENTATION PAGE			Form Approved OMB No. 0704-0188	
Public reporting burden for this collection of information is estimated to average 1 hour per response, including the time for reviewing instruction, searching existing data sources, gathering and maintaining the data needed, and completing and reviewing the collection of information. Send comments regarding this burden estimate or any other aspect of this collection of information, including suggestions for reducing this burden, to Washington headquarters Services, Directorate for Information Operations and Reports, 1215 Jefferson Davis Highway, Suite 1204, Arlington, VA 22202-4302, and to the Office of Management and Budget, Paperwork Reduction Project (0704-0188) Washington DC 20503.				
1. AGENCY USE ONLY (Leave blank)		2. REPORT DATE December 2006	3. REPORT TYPE AND DATES COVERED Master's Thesis	
4. TITLE AND SUBTITLE: Variable Resolution Direction Finding Using the Robust Symmetrical Number System			5. FUNDING NUMBERS	
6. AUTHOR(S) Anthony Lee				
7. PERFORMING ORGANIZATION NAME(S) AND ADDRESS(ES) Center for Joint Services Electronic Warfare Naval Postgraduate School Monterey, CA 93943-5000			8. PERFORMING ORGANIZATION REPORT NUMBER	
9. SPONSORING /MONITORING AGENCY NAME(S) AND ADDRESS(ES) Office of Naval Research Arlington, V.A.			10. SPONSORING/MONITORING AGENCY REPORT NUMBER	
11. SUPPLEMENTARY NOTES The views expressed in this thesis are those of the author and do not reflect the official policy or position of the Department of Defense or the U.S. Government.				
12a. DISTRIBUTION / AVAILABILITY STATEMENT Approved for public release; distribution is unlimited			12b. DISTRIBUTION CODE	
13. ABSTRACT (maximum 200 words) A digital implementation of a phase sampling interferometer antenna system based on the Robust Symmetrical Number System (RSNS) is built using commercial-off-the-shelf (COTS) items. The RSNS-based direction finding (DF) system uses short baselines to achieve a high resolution DF capability in a physically compact system for use as stand-in sensors on unmanned aerial vehicles. The RSNS inherent integer Gray code property minimizes the possible encoding errors and adds a robustness to the accuracy of the estimated Angle of Arrival (AOA). A digital architecture using quadrature demodulators and real-time controllers provide greater flexibility for signal processing and allows for the implementation of a new virtual spacing algorithm. The virtual spacing concept changes the RSNS moduli values to implement a virtual antenna spacing without having to physically change the antenna element spacing. This enables higher resolution DF in circumstances where the Signal-to-Noise Ratio (SNR) is high enough to provide error free coding of the AOA. Two four element, digital 3-channel interferometer prototype systems were constructed and tested in the NPS anechoic chamber. The first antenna array is designed using pairwise relatively prime (PRP) moduli. When an extension of the virtual spacing concept for application to N-channel systems was successfully resolved, a second 3-channel array was built using non-PRP moduli for evaluating the performance of the virtual spacing concept. The simulated and experimental results, hardware implementation and testing procedures are presented in this thesis. Results for the first array show that the RSNS-based DF system is able to provide 0.7 degree RMS resolution with a baseline of 66 cm. For the second virtual spacing array, the short physical baseline of 14 cm was sensitive to noise and antenna spacing errors.				
14. SUBJECT TERMS Direction Finding, Robust Symmetrical Number System, Variable Resolution, Transmitter, Receiver, COTS, Quadrature Modulator, Quadrature Demodulator, Demonstration Array, High Resolution			15. NUMBER OF PAGES 119	
			16. PRICE CODE	
17. SECURITY CLASSIFICATION OF REPORT Unclassified	18. SECURITY CLASSIFICATION OF THIS PAGE Unclassified	19. SECURITY CLASSIFICATION OF ABSTRACT Unclassified	20. LIMITATION OF ABSTRACT UL	

THIS PAGE INTENTIONALLY LEFT BLANK

Approved for public release; distribution is unlimited.

**VARIABLE RESOLUTION DIRECTION FINDING USING THE ROBUST
SYMMETRICAL NUMBER SYSTEM**

Anthony Lee Kok Long
Major, Republic of Singapore Navy
B.S., University of Tasmania, 1999

Submitted in partial fulfillment of the
requirements for the degree of

**MASTER OF SCIENCE IN COMBAT SYSTEMS SCIENCES AND
TECHNOLOGY**

from the

**NAVAL POSTGRADUATE SCHOOL
December 2006**

Author: Anthony Lee

Approved by: Phillip E. Pace
Thesis Advisor

David C. Jenn
Thesis Advisor

Donald L. Walters
Thesis Advisor

James H. Luscombe
Chairman, Department of Physics

THIS PAGE INTENTIONALLY LEFT BLANK

ABSTRACT

A digital implementation of a phase sampling interferometer antenna system based on the Robust Symmetrical Number System (RSNS) is built using commercial-off-the-shelf (COTS) items. The RSNS-based direction finding (DF) system uses short baselines to achieve a high resolution DF capability in a physically compact system for use as stand-in sensors on unmanned aerial vehicles. The RSNS inherent integer Gray code property minimizes the possible encoding errors and adds a robustness to the accuracy of the estimated Angle of Arrival (AOA).

A digital architecture using quadrature demodulators and real-time controllers provide greater flexibility for signal processing and allows for the implementation of a new *virtual spacing* algorithm. The virtual spacing concept changes the RSNS moduli values to implement a virtual antenna spacing without having to physically change the antenna element spacing. This enables higher resolution DF in circumstances where the Signal-to-Noise Ratio (SNR) is high enough to provide error free coding of the AOA.

Two four element, digital 3-channel interferometer prototype systems were constructed and tested in the NPS anechoic chamber. The first antenna array is designed using pairwise relatively prime (PRP) moduli. When an extension of the virtual spacing concept for application to N-channel systems was successfully resolved, a second 3-channel array was built using non-PRP moduli for evaluating the performance of the virtual spacing concept. The simulated and experimental results, hardware implementation and testing procedures are presented in this thesis. Results for the first array show that the RSNS-based DF system is able to provide 0.7 degree RMS resolution with a baseline of 66 cm. For the second virtual spacing array, the short physical baseline of 14 cm was sensitive to noise and antenna spacing errors.

THIS PAGE INTENTIONALLY LEFT BLANK

TABLE OF CONTENTS

I.	INTRODUCTION.....	1
A.	RADIO DIRECTION FINDING INTERFEROMETRY	1
B.	PREVIOUS WORK.....	2
C.	THESIS OBJECTIVE	3
D.	PRINCIPAL CONTRIBUTIONS	3
E.	THESIS ORGANIZATION.....	4
II.	DIRECTION FINDING BY PHASE INTERFEROMETRY	7
A.	THEORY OF PHASE INTERFEROMETRY	7
B.	AMBIGUITIES IN PHASE INTERFEROMETRY	9
C.	SUMMARY	11
III.	ROBUST SYMMETRICAL NUMBER SYSTEM-BASED DIRECTION FINDING	13
A.	THE ROBUST SYMMETRICAL NUMBER SYSTEM.....	13
B.	THE RSNS ANTENNA ARCHITECTURE.....	16
1.	Applying Rsns to Interferometers	17
2.	Resolution of the RSNS Interferometer	20
C.	DESIGN EXAMPLE AND EXPERIMENTAL RESULTS	20
1.	Design of the DF System.....	21
2.	Experimental Results and Analysis	25
D.	SUMMARY	26
IV.	DESIGN OF RSNS-BASED DF DEMONSTRATION ARRAY – DETERMINING RSNS PARAMETERS	27
A.	DETERMINING RSNS PARAMETERS	27
B.	STIMULATION RESULTS FOR DF ARRAY USING MODULI {7 15 29}	30
C.	SUMMARY	34
V.	DESIGN OF RSNS-BASED DF DEMONSTRATION ARRAY – HARDWARE AND SOFTWARE IMPLEMENTATION	37
A.	HARDWARE DESIGN	37
B.	OVERVIEW OF HARDWARE COMPONENTS	38
1.	Dipole Antenna Element.....	39
2.	Ground Plane	42
3.	Low Noise Amplifiers (LNA-2700)	42
4.	RG-303 Cables	44
6.	Power Splitter.....	51
7.	RG-58 Cable	51
8.	National Instrument Modules.....	51
9.	Power Supply Unit	53
C.	IMPLEMENTING AND TESTING RSNS ALGORITHM IN LABVIEW.....	54
D.	SUMMARY	59

VI.	RESULTS AND ANALYSIS – ANTENNA ARRAY USING MODULI {7 15 29}.....	61
A.	CALIBRATION AND PREPARATION TESTS	61
1.	Centering I/Q Response of Demodulator Boards	61
2.	Rotation of Phase Response in Demodulator Boards.....	61
3.	Noise of Demodulator Boards	62
4.	Power of Local Oscillator Input to Demodulator Board	62
B.	INITIAL TESTS AT ANECHOIC CHAMBER	63
1.	Alignment of the Array	63
2.	Construction of Anechoic Chamber and RF Reflections ...	64
3.	Demodulator Rotation Calibration	65
4.	Phase Differentials on Changing Signal AOA.....	65
5.	Plane Approximation of Spherically Propagating RF Signal.....	65
C.	TROUBLESHOOTING AT MICROWAVE LAB	66
1.	Demodulator Operating Mode	66
2.	Defective Components.....	66
D.	SECOND ROUND OF ANECHOIC CHAMBER TESTS	67
E.	THIRD ROUND OF ANECHOIC CHAMBER TESTS.....	69
1.	Raising the DF Array Platform.....	69
2.	Grounding Unused Demodulator Terminals	70
3.	Shielding for DF Array.....	70
4.	Aligning DF Array with Transmit Antenna.....	71
F.	UPDATING HMI AND IN-DEPTH DF PERFORMANCE.....	74
1.	Updating Human Machine Interface.....	74
2.	Detailed DF Performance	75
G.	SUMMARY	76
VII.	RSNS INTERFEROMETRY WITH VIRTUAL SPACING	77
A.	TWO CHANNEL RSNS INTERFEROMETRY WITH VIRTUAL SPACING	77
B.	N-CHANNEL RSNS INTERFEROMETRY WITH VIRTUAL SPACING	79
C.	VIRTUAL SPACING COMBINATIONS FOR N-CHANNEL SYSTEMS	82
D.	DESIGN EXAMPLE FOR 3-CHANNEL RSNS INTERFEROMETRY WITH VIRTUAL SPACING	82
E.	BUILDING AND TESTING THE VIRTUAL SPACING DF SYSTEM..	85
F.	ERROR SOURCES FOR THE VIRTUAL ARRAY	90
1.	Plane Wave Approximation.....	90
2.	Demodulator Phase Errors	90
3.	Antenna Spacing Errors.....	90
G.	LIMITATIONS AND CHALLENGES OF APPLYING VIRTUAL SPACING	91
1.	Scaling Factor and Resulting FOV.....	91
2.	SNR to Support Error Free Coding.	91

3.	Coding Errors and the Probability of Correct Bin Estimation.	91
H.	SUMMARY AND ANALYSIS OF DF PERFORMANCE	92
VIII.	CONCLUSIONS AND RECOMMENDATIONS.....	93
A.	SENSITIVITY ANALYSIS	93
B.	REDUCING MAIN ERROR SOURCES.....	94
1.	Demodulator Board	94
2.	Antenna Spacing	94
3.	Plane Wave Approximation.....	95
C.	OTHER PERMUTATIONS FOR VIRTUAL SPACING	95
1.	Combination of Real Spacing for Virtual Spacing	95
2.	Optimizing the Choice of Virtual Spacing Used.....	95
3.	Virtual Spacing for PRP Moduli Sets	96
D.	EXTENSION OF DEMONSTRATION ARRAY FOR WIDEBAND APPLICATIONS.....	96
	LIST OF REFERENCES.....	97
	INITIAL DISTRIBUTION LIST	99

THIS PAGE INTENTIONALLY LEFT BLANK

LIST OF FIGURES

Figure 1.	Basic Phase-delay / Time-delay Interferometry (After[2]).	2
Figure 2.	Two-Element Interferometry (After [2]).	7
Figure 3.	Phase Differential vs AOA for $d=\lambda/2$ (After [7]).	9
Figure 4.	Phase Differential vs AOA for $d=\lambda$ (After [7]).	10
Figure 5.	Output Voltage vs AOA for (a) $d=\lambda/2$ and (b) $d=\lambda$ (After [3]).	16
Figure 6.	Mapping RSNS folding waveforms to threshold values (After [4]).	19
Figure 7.	Block diagram of the RSNS-based DF System (From [5]).	21
Figure 8.	Folding Output Waveforms with Phase Adjustment (From [7]).	24
Figure 9.	Phase Adjusted Folding Waveforms after Comparators (From [7]).	24
Figure 10.	Transfer Function, the Estimated AOA versus Actual AOA (From [7]).	25
Figure 11.	Measured RSNS Transfer Function (From [5]).	26
Figure 12.	Transfer Function for Demonstration Array using Moduli {7 15 29}.	30
Figure 13.	Transfer Function Near Broadside.	31
Figure 14.	Transfer Function at High AOA Angles.	32
Figure 15.	Quantization Error for Demonstration Array.	33
Figure 16.	Quantization Error Near Broadside.	33
Figure 17.	Quantization Error at High AOA Angles.	34
Figure 18.	Hardware Block Diagram of Demonstration Array.	38
Figure 19.	Two Dipole Elements, One Mounted in a Ground Plane (From [13]).	40
Figure 20.	Dipole element pattern measurement measured at 2.40 GHz (From [12]).	41
Figure 21.	Low-Noise amplifier LNA-2700 from RF Bay, Inc.	42
Figure 22.	Quadrature Type Demodulation of 2-Channel Interferometer (After [7]).	45
Figure 23.	Basic Quadrature Demodulation Processing (After [7]).	46
Figure 24.	AD8347EVAL wiring connections and mode settings (From [13]).	48
Figure 25.	Plotted AD8347 Demodulator Phase Characteristics (From [12]).	50
Figure 26.	NI Modular Systems Used for Demonstration Array	52
Figure 27.	LabView 8.0 – Main Control Software.	53
Figure 28.	Dual-Output Power Supply Unit.	54
Figure 29.	Block Diagram for RSNS Signal Processing.	55
Figure 30.	HMI for Initial Development (LabView Front Panel).	56
Figure 31.	LabView Simulator for RSNS-Algorithm (Front Panel).	57
Figure 32.	LabView Block Diagram for LabView Simulator.	58
Figure 33.	LabView Block Diagram after Combining both Vis.	59
Figure 34.	Testing of Demonstration Array in Anechoic Chamber.	64
Figure 35.	Plan View Showing Plane Wave Approximation.	65
Figure 36.	Initial Results from Demonstration Array.	68
Figure 37.	Initial Results – AOA Estimation Error.	68
Figure 38.	Front View of DF System on Pedestal.	69
Figure 39.	Grounding Unused Demodulator Terminals.	70

Figure 40.	Shielding for DF System.....	71
Figure 41.	Aligning DF Array to Transmit Antenna.	71
Figure 42.	AOA Estimation Error – 2 nd Set of Results.	73
Figure 43.	Updated HMI with Write-to-File Capability.....	75
Figure 44.	DF Performance – 3 rd Set of Results.....	76
Figure 45.	Transfer Function of Real Spacing using Moduli {4 8 16}.....	84
Figure 46.	Transfer Function of Virtual Spacing using Moduli {3 9 18}.....	84
Figure 47.	Transfer Function of Virtual Spacing using Moduli {9 27 54}.....	85
Figure 48.	Antenna Array for 3-Channel Virtual Spacing Concept.....	86
Figure 49.	Simplified Flow Diagram for Virtual Spacing Signal Processing.	87
Figure 50.	LabView Simulator for Virtual Spacing.	88
Figure 51.	DF Experimental Performance for Virtual Spacing Array.....	89

LIST OF TABLES

Table 1. RSNS Sequence for $m_1 = 3$ ($s_1 = 0$) and $m_2 = 4$ ($s_2 = 1$) (After [7]).	14
Table 2. RSNS Sequence for $m_1=8$ and $m_2=17$ (From [3]).	22
Table 3. Threshold Values for Moduli set {8 17} (From [5]).	23
Table 4. Threshold Values for Demonstration Array.	29
Table 5. Phase Adjustment Terms for Demonstration Array.	30
Table 6. List of Hardware Components.	39
Table 7. LNA-2700 Specifications (From [15]).	43
Table 8. Gain and Response of LNAs.	43
Table 9. Gain and Phase Response of RG-303 Cables.	44
Table 10. Modifications Made to Operate the AD8347 Demodulator in VGIN Mode (After [13]).	49
Table 11. AD8347 Phase Response.	50
Table 12. Parameters of Power Splitter.	51
Table 13. Initial Results from Demonstration Array.	67
Table 14: DF Performance – 2 nd Set of Results	72
Table 15. Moduli Sets for 3-Channel Virtual Array.	83
Table 16: Moduli Sets for 3-Channel Virtual Spacing Concept.	86

THIS PAGE INTENTIONALLY LEFT BLANK

ACKNOWLEDGMENTS

First of all I would like to express my gratitude to the Singapore Navy for providing me the opportunity to further my technical expertise at the renowned Naval Postgraduate School. NPS is truly a unique institution where multi-disciplines are blended with a view for military applications.

It has been a great pleasure and honor to work with Professor David C. Jenn, Professor Phillip E. Pace and Professor Donald Walters. I would like to express my appreciation for your patience, guidance and invaluable support in the overcoming the stumbling blocks that were faced along the journey.

I am deeply grateful to Robert D. Broadston, Lab Director of the Microwave Lab. He has always been there to assist us in tackling problems and to offer practical suggestions on the next step to making the project work. His enthusiasm and expertise provided me with the confidence that we would prevail against the barrage of challenges that COTS perpetually presented to us. His resourcefulness is uncanny and inspiring.

When I started the thesis work April 2006, two other thesis students, Gert Burgstaller and Levent Gezer, graduating in September 2006, were working with Prof Jenn on their respective thesis. Their work used several identical hardware components and the same software (LabView 8.0) for the controlling the hardware. I would like to thank them for their assistance at the initial stages for lessening the challenges of a steep learning curve.

I would like to thank William Bigas and Paul M. Eyring, from EDO Corporation, for taking the time to come to NPS to have a look at the demonstration DF system. They provided great suggestions and insights that would pave the way for development of the RSNS-based system for real-life applications.

Finally and most importantly, I would like to thank my dearest wife, Eileen, and my children, Charmaine and Christopher, for being my pillars of strength. Thank you, Eileen, for your ardent support and for taking fantastic care of our family during our stay here.

I. INTRODUCTION

A. RADIO DIRECTION FINDING INTERFEROMETRY

Radio direction finding (DF) has numerous applications in a variety of fields such as navigation, disaster response, wildlife tracking and electronic warfare. In the military context, DF forms an important branch of electronic intelligence (ELINT). DF systems enable the tracking of radiating platforms, for example, by means of triangulation, whereby appropriately spaced DF systems determine the geo-location of the radiating platform by combining the Angle-of-Arrival (AOA) information from the known positions of the DF systems.

DF systems are designed (and categorized) based on how they measure the characteristics of the intercepted electromagnetic (EM) signal to determine the AOA. There are three broad categories: amplitude comparison, phase interferometry and time interferometry [1]. Some systems employ algorithms that utilize a combination of measurements. The use of both amplitude comparison in combination with time or phase interferometry is common.

Amplitude comparison systems extract the amplitude response of the antenna elements to determine the AOA. The directional properties of elemental H-field loops and E-field dipoles provide response minima as they are rotated in azimuth. AOA estimates are acquired at these minima response orientations.

Time and phase interferometry DF systems operate on a similar principle. Antenna arrays with multiple elements are placed at pre-determined distances based on the required resolution and frequency of the emitter to be intercepted. Given that EM waves require a finite time to traverse the distance between the antenna elements, the time or phase difference between elements can be measured to determine the AOA of the emitter. This treatment approximates the EM wave-front to be planar, which is reasonable in most applications, as DF systems usually operate in the far-field of the source.

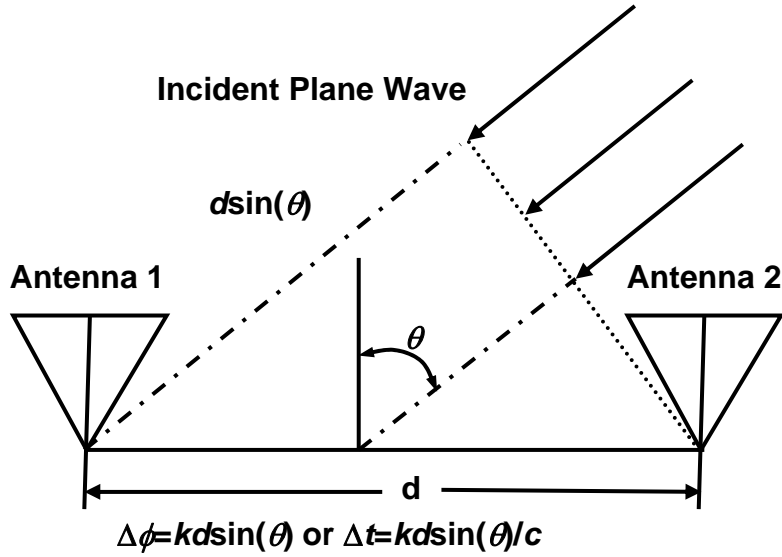


Figure 1. Basic Phase-delay / Time-delay Interferometry (After[2]).

Phase interferometry systems can generate an AOA resolution of ± 1 degree, which satisfies modern electronic warfare (EW) requirements [2]. To achieve high resolution, the antenna element spacing is increased. When antenna element spacing is increased beyond the half-wavelength distance, the inherent challenge of resolving the ambiguities presents itself as more than one unique solution is available. This challenge can be overcome by introducing auxiliary antenna elements, where the large baselines provide high resolution, and small baselines are used to overcome ambiguities.

B. PREVIOUS WORK

This research is part of an ongoing project to apply the RSNS algorithm in the area of direction finding to achieve the dual advantage of high resolution and small baselines. The previous implementations [3,4] used EEPROMS and mixed signal processing respectively to perform the RSNS signal processing. The results were promising but contained a large number of encoding errors, due to noise and errors that could not be corrected due to the analog architecture used. Subsequent results [5] showed substantial improvements, but had several ‘fading’ regions where large errors existed.

In [6], the use of digital antenna architectures using COTS items was investigated. In [7], a 'virtual channel' concept using virtual element spacing was introduced. Simulations showed that a variable resolution signal processing approach could be applied to the RSNS DF signal processing architecture for two-channel systems.

C. THESIS OBJECTIVE

Previous work dealt largely with simulations and the implementation was constructed using a 2-channel analog system. The research goal is to expand on the previous work by designing and building a 3-channel demonstration array using a digital architecture. A test-bed DF system for intercepting continuous wave (CW) signals at 2.4 GHz was built entirely out of low-cost COTS equipment and subsequently used to evaluate the high resolution RSNS and the 'virtual channel' concept.

The objectives of this thesis are threefold:

1. Design of a demonstration, 3-channel DF array, based on RSNS theory and implemented using a digital architecture.
2. Evaluation of high resolution RSNS coding using COTS equipment.
3. Evaluation of 'Virtual Channel' concept and the analytical extension for N-channel systems.

D. PRINCIPAL CONTRIBUTIONS

The design steps and application of RSNS algorithm to direction finding was simplified into eight steps. MATLAB scripts have also been compiled into a single program for simulations. A MATLAB script was written specifically for the generation of key RSNS parameters, including the look up table, for use in a LabView controlling program.

All hardware design and specifications and the development process of the DF system are clearly captured in the thesis. Test setup and procedures,

including calibration values, are also tabulated for conducted tests to be replicated if necessary. The test results, as well as challenges and errors that were made, are listed in the thesis chronologically.

One key contribution is the extension of the virtual spacing concept for N-channel DF systems. Initial tests have been conducted for a three-channel system using virtual spacing. With all hardware and controlling software for a 3-channel DF system fully developed and functional, research into the application of wideband virtual spacing DF systems can be continued with ease.

E. THESIS ORGANIZATION

Chapter II reviews the basic operating principles of phase interferometry DF systems and provides the fundamental basis for applying RSNS for direction finding.

Chapter III explains the RSNS theory and its application to phase interferometry. The process of designing a RSNS-based DF system is presented. Results from previous research and experiments are also presented.

Chapter IV and V present the design and development of the DF system using COTS equipment. Chapter IV deals with parametric design and calculations for building a 3-channel DF array based on RSNS theory. Simulation results from MATLAB are presented. Chapter V presents the overview of the hardware used for building the demonstration array and software development of the control program using the NI-LabView program.

Chapter VI presents, in chronological order, the observations and results of tests conducted on the demonstration array. Analysis of the results and possible error sources are identified and discussed.

Chapter VII covers the previous work on virtual spacing for 2-channel DF systems. This concept is then extended for applications for N-Channel systems. Simulation and test results for a 3-channel virtual spacing DF system are presented.

Finally, Chapter VIII presents the conclusions and offer exciting possibilities for future work in this research field.

THIS PAGE INTENTIONALLY LEFT BLANK

II. DIRECTION FINDING BY PHASE INTERFEROMETRY

This chapter reviews the basic operating principles of DF by means of phase interferometry using an analog implementation.

A. THEORY OF PHASE INTERFEROMETRY

It is important to note that the following treatment assumes that the DF array is in the 'far-field' with respect to the emitter. This is often the case for practical DF systems as the DF array would be sufficiently far from the emitter to approximate the wave-front as a planar wave.

A basic one-channel linear interferometer is shown in Figure 2. It is comprised of two identical antenna elements, spaced d apart. The incident EM wave arrives at an angle θ , measured from the perpendicular to the baseline axis. The angle θ takes on the values from -90° to 90° .

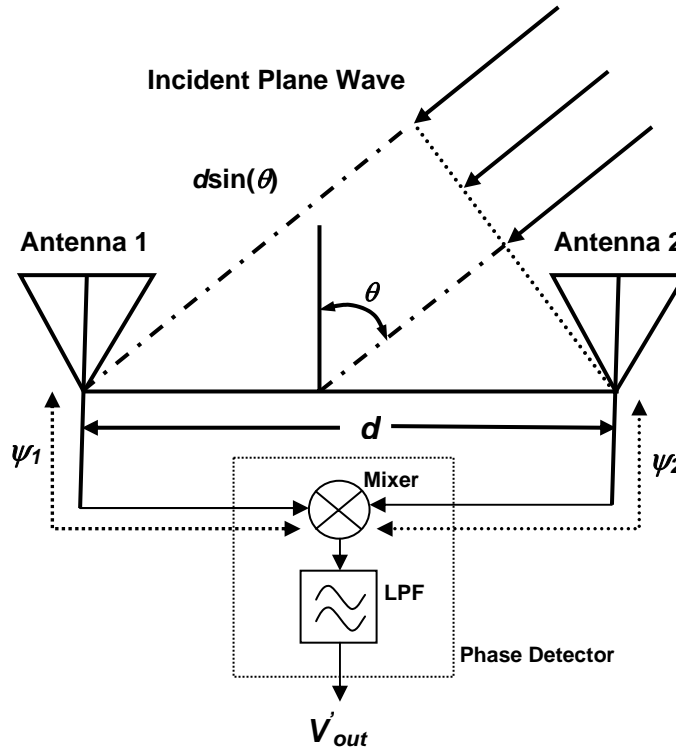


Figure 2. Two-Element Interferometry (After [2]).

The incident wave arrives at antenna element 1 and after propagating an additional distance of $d \sin(\theta)$, arrives at element 2. The signals from the two antenna elements take on the following form:

$$V_i = V \cos(\omega_c t + \psi_i + \phi_i) \quad (2.1)$$

where i denotes the element index number; V is the signal amplitude response, ω_c is the signal frequency in radians/sec, ψ_i is the phase term due to propagation in the cables and ϕ_i is the phase term relative to the origin. In an analog architecture, the signals from the antennas are fed into a mixer and low-pass-filter (LPF). This system, commonly known as a phase detector, produces an output voltage of the following form:

$$V_{out}(\phi) = \frac{V^2}{2} \cos(\Delta\psi + \Delta\phi) \quad (2.2)$$

where $\Delta\psi$ results from the phase differential due to cable length differences, and $\Delta\phi$ results from the phase differential due to the additional $d \sin(\theta)$ distance traveled by the signal wave-front to reach antenna element 2. This can be re-written in the following form:

$$V_{out}(\phi) = \frac{V^2}{2} \cos(\Delta\psi + kd \sin(\theta)) \quad (2.3)$$

where $k = \frac{2\pi}{\lambda}$ is the wavenumber.

After eliminating the cable phase differential component and normalizing the output voltage to unit amplitude, we arrive at the following output

$$V_{out}(\phi) = \cos(kd \sin(\theta)) \quad (2.4)$$

The phase differential $kd \sin(\theta)$ takes on the value of $-\pi$ to π and repeats itself with a period of 2π .

B. AMBIGUITIES IN PHASE INTERFEROMETRY

The phase differential $\Delta\phi$ is a function of the AOA, frequency and distance between the antenna elements. The phase differential is periodic and repeats itself with a period of 2π . This leads to ambiguities at high frequencies or with a large spacing between the antenna elements.

When antenna element spacing is $d \leq \lambda/2$, a one to one mapping between the AOA and the phase differential exists. Consider the case of $d = \lambda/2$. The phase differential is given by $\Delta\phi = \pi \sin(\theta)$ radians. Figure 3 shows the phase differential versus AOA in degrees, with a one to one mapping without ambiguities.

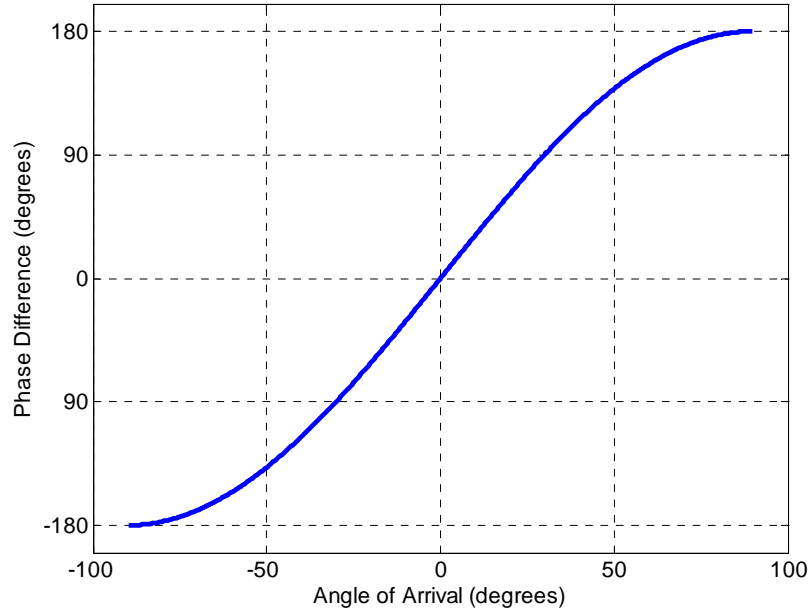


Figure 3. Phase Differential vs AOA for $d=\lambda/2$ (After [7]).

One measure of resolution, which is the precision at which we can measure the AOA, is defined as the phase gain or the rate of change of the phase differential versus the AOA [1]. The unit is degrees per degree. In Figure 3, the phase gain is 2 degrees per degree change in AOA.

Ambiguities occur when the spacing between antenna elements is greater than half of the frequency wavelength $d \geq \lambda/2$. Now consider the case where the antenna spacing is increased to one wavelength. Now $d=\lambda$ and the phase differential is given by $\Delta\phi = 2\pi \sin(\theta)$ radians. In this case, the phase differential completes exactly one rotation as the wave travels over the distance of one wavelength as shown in Figure 4. Phase gain has increased by a factor of 2, to 4 degrees in phase differential for every degree change in AOA, in proportion with the increase in element distance.

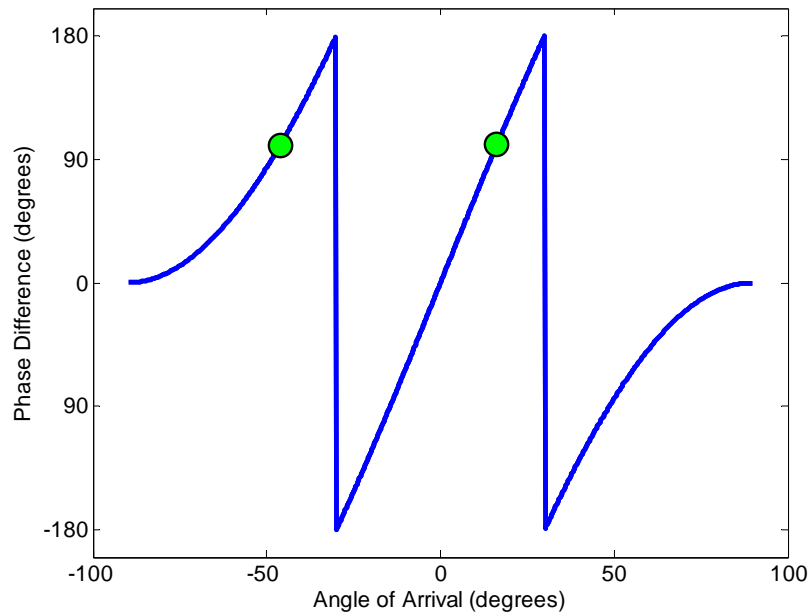


Figure 4. Phase Differential vs AOA for $d=\lambda$ (After [7]).

The phase differential now suffers from ambiguities. The mapping from AOA to phase differential is no longer unique. Solving for the AOA using the same phase differential presents us with two possible AOA answers.

Increasing the antenna element spacing increases the resolution but also proportionally increases the phase ambiguities that must be resolved. In practice, a phase interferometry system has several baselines, where the long baselines provide the resolution and the short baselines are used to resolve the ambiguities.

C. SUMMARY

We have covered the principles of basic phase interferometry and AOA ambiguities resulting from high frequency or large antenna element spacing. In the next chapter, we will review the Robust Symmetric Number System and how it can efficiently resolve the phase ambiguities in high resolution phase interferometry.

THIS PAGE INTENTIONALLY LEFT BLANK

III. ROBUST SYMMETRICAL NUMBER SYSTEM-BASED DIRECTION FINDING

Since it is desirable to obtain high resolution AOA estimates without a long baseline, a signal processing method employing the robust symmetrical number system (RSNS) was introduced in [3, 4, 5, 7]. In this chapter, the RSNS theory is reviewed and a step by step implementation for phase interferometry is discussed. Previous experimental data are also presented and discussed.

A. THE ROBUST SYMMETRICAL NUMBER SYSTEM

1. Basic Properties of the RSNS

Consider an N -channel RSNS, where $N > 1$. The basic RSNS sequence has the following form [8]:

$$\{x_h\} = [\underbrace{0, 0, \dots, 0}_N, \underbrace{1, 1, \dots, 1}_N, \dots, \underbrace{m_i - 1, \dots, m_i - 1}_N, \underbrace{m_i, \dots, m_i}_N, \underbrace{m_i - 1, \dots, m_i - 1}_N, \dots, \underbrace{1, \dots, 1}_N] \quad (3.1)$$

$$\{x_h\} = \begin{cases} \left\lfloor \frac{h - s_i}{N} \right\rfloor & s_i \leq h \leq Nm_i + s_i + 1 \\ \left\lfloor \frac{2Nm_i + N - h + s_i - 1}{N} \right\rfloor & Nm_i + s_i + 2 \leq h \leq 2Nm_i + s_i - 1 \end{cases} \quad (3.2)$$

In Equation (3.1), each sequence corresponding to m_i , is shifted either left or right by $s_i = i - 1$ placed for $i \in \{1, \dots, N\}$. The shift values $\{s_1, s_2, \dots, s_N\}$ must form a complete residue system modulo N in order to realize the RSNS integer Gray-code properties. Equation (3.2) determines the discrete state of each sequence.

It has been shown that the period of a single channel with modulus m_i is [9]

$$P_{RSNS} = 2Nm_i \quad (3.3)$$

and the fundamental period of an N -channel RSNS with modulus set (m_1, m_2, \dots, m_N) is

$$PF_{RSNS} = 2N(m_1, m_2, \dots, m_N) \quad (3.4)$$

where (m_1, m_2, \dots, m_N) represents the least common multiple of m_1, m_2, \dots, m_N .

2. Determining the Dynamic Range of a RSNS Sequence

Consider the two modulus set $\{3, 4\}$ where for $m_1 = 3$ ($s_1 = 0$) and $m_2 = 4$ ($s_2 = 1$). In this example, the shift is to the right. Table 1 shows the RSNS sequence with the appropriate shift applied to the modulus. The column vectors, which consist of the integers within each modulus, change one at a time between code positions and possess integer Gray-code properties.

h	0	1	2	3	4	5	6	7	8	9	10	11	12	13	14	15	16	17	18	19
$m_1 = 3$ ($s_1 = 0$)	0	1	1	2	2	3	3	2	2	1	1	0	0	1	1	2	2	3	3	2
$m_2 = 4$ ($s_2 = 1$)	0	0	1	1	2	2	3	3	4	4	3	3	2	2	1	1	0	0	1	1
\hat{M}					0	1	2	3	4	5	6	7	8	9	10	11	12	13	14	

Table 1. RSNS Sequence for $m_1 = 3$ ($s_1 = 0$) and $m_2 = 4$ ($s_2 = 1$) (After [7]).

Searching along the vector from left to right, we wish to find the largest continuous set of column vectors that are distinct. This sequence of distinct vectors forms the unambiguous output of the system and is defined as the system dynamic range, denoted by \hat{M} . In [10], it was proved that the selection of the sequence shift (s_i) and permutations among the moduli has no effect on \hat{M} , but may produce different start and stop points for the vectors corresponding to \hat{M} . The dynamic range of the 2-channel example shown in Table 1 is $\hat{M} = 15$.

The dynamic range of several particular moduli combinations have been formulated in closed form. For two channels, three combinations of two relatively prime moduli m_1 and m_2 can yield \hat{M} as follows [11]:

Case I: $m_1 \geq 3$ and $m_2 = m_1 + 1$, then

$$\hat{M} = 3(m_1 + m_2) - 6 \quad (3.7)$$

Case II : $m_1 \geq 5$ and $m_2 = m_1 + 2$, then

$$\hat{M} = 3(m_1 + m_2) - 7 \quad (3.8)$$

Case III : $m_1 \geq 5$ and $m_2 = m_1 + C$, and $C \geq 3$, then

$$\hat{M} = 4m_1 + 2m_2 - 2 \quad (3.9)$$

Checking the example shown in Table 1, which fits Equation (3.7), yields

$$\hat{M} = 15.$$

For three channel systems, two combinations with closed form solutions are available [9, 10]:

Case I: $m_1 = 2^k - 1$, $m_2 = 2^k$, $m_3 = 2^k + 1$ for $m_1 \geq 3$, then

$$\hat{M} = \frac{3}{2}m_1^2 + \frac{15}{2}m_1 + 7 \quad (3.7)$$

Case II : $m_2 = 2m_1 + 1$, $m_3 = 4m_1 + 1$, then

$$\hat{M} = 6m_1^2 + 21m_1 + 3 \quad (3.8)$$

For other cases, a computer search algorithm would prove to be the most efficient means of determining the dynamic range and its vector sets, especially when dealing with large modulus numbers and channels [7, 10].

So far, we have reviewed the basic features of the RSNS. In the next section, the relationship between RSNS theory and DF systems is discussed.

B. THE RSNS ANTENNA ARCHITECTURE

The output voltage of the interferometer between two elements is given by $V_{12}(\phi) = \cos(kd_1 \sin(\theta)) = \cos(\Delta\phi_{12})$. For illustration, the normalized output voltage for the cases of $d=\lambda/2$ and $d=\lambda$ are plotted in Figure 5.

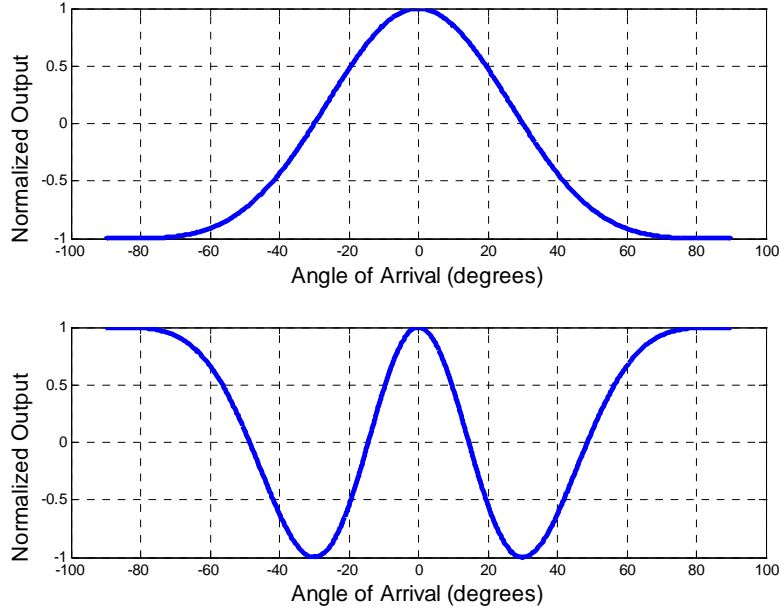


Figure 5. Output Voltage vs AOA for (a) $d=\lambda/2$ and (b) $d=\lambda$ (After [3]).

The plots show that the waveforms are symmetrical about the origin (the broadside of the array). The ‘visible region’ in this case is the AOA over -90 to $+90$ degrees. The waveform also appears in ‘folds’ over the visible region. The number of folds for a given frequency and antenna element spacing are given by

$$n = \frac{d}{\lambda/2} = \frac{2d}{\lambda} \quad (3.9)$$

By increasing element distances by a factor of two and shifting the output folding waveform to be symmetric about the origin, a binary resolution interferometer system can be designed.

1. Applying Rsns to Interferometers

To apply the concept of RSNS-based signal processing to interferometers, a robust symmetrical number sequence with a proper shift value is used to represent a symmetrical folding waveform out of the antenna. The following describes the steps required to integrate the RSNS signal processing into a phase interferometer DF system.

a. *Determine N , the number of channels required.* The number of required antenna elements will be $N+1$.

b. *Identify an integer valued modulus for each channel ($m_1, m_2 \dots m_i$).* It has been shown that choosing pairwise relatively prime (PRP) moduli such as {3 7} and {7 19} gives the most efficient dynamic range.

c. *Determine the system dynamic range based on the chosen moduli.* This can be extremely time consuming when dealing with large modulus values and large number of channels. A MATLAB-based search algorithm has been developed by [7, 10] to facilitate this process.

d. *Define the number of folds within each modulus.* This is calculated by dividing the dynamic range by the period of each modulus.

$$n_i = \frac{\hat{M}}{P_{RSNS}} = \frac{\hat{M}}{2Nm_i} \quad (3.10)$$

e. *Determine the required antenna spacing for each channel.*

$$d_i = n_i \frac{\lambda}{2} = \frac{\hat{M}\lambda}{4Nm_i} \quad (3.11)$$

f. *Re-mapping the Field of View (FOV).* **This is an optional step.** Antenna patterns degrade at wide angles. The reliable-FOV characteristics of the antenna elements chosen for implementing the antenna array should be determined, and the RSNS-FOV can be compressed by means of a scaling factor to cover the reliable antenna FOV. This has the effect of

enhancing resolution and decreasing the required antenna spacing [12]. Considering Equation (2.4) with k and V_{out} held constant, we have

$$d \sin(\theta) = d' \sin(\theta') \quad (3.12)$$

where θ and d correspond to the maximum field of view (FOV) and the antenna spacing for the original (unscaled) configuration. The quantities θ' and d' are the maximum FOV and antenna spacing for the remapped (scaled) configuration. Rearranging Equation (3.12), the scale factor is defined as

$$\xi = \frac{d'}{d} = \frac{\sin(\theta)}{\sin(\theta')} \quad (3.13)$$

Combining Equations (3.11) and (3.13), we obtain the scaled antenna spacing

$$d'_i = d_i \xi = \frac{\hat{M} \lambda}{4m_i N} \xi \quad (3.14)$$

g. *Determine the thresholds.* In the digital architecture, the thresholds can be implemented by means of a program or script. The thresholds for channel m_i are

$$V_{j,m_i} = \cos \left(\frac{m_i - j + \frac{1}{2}}{m_i} \pi \right), \quad 1 \leq j \leq m_i \quad (3.15)$$

When a folding waveform exceeds a threshold, the integer value within the RSNS sequence increments; likewise the integer value decrements when the folding waveform drops below a threshold. Figure 6 illustrates the discrete states of the two-channel RSNS example as shown in Table 1. The symmetrical folding waveforms having moduli $m_1=3$ ($s_1=0$) and $m_2=4$ ($s_2=1$) are superimposed with the thresholds V_{j,m_i} from Equation (3.15), shown on the vertical axis. This encodes the folding waveforms into the RSNS. The discrete states (integers) shown above the folding waveforms represent the number of thresholds crossed by the folding waveform. Note that only one threshold is crossed at a time.

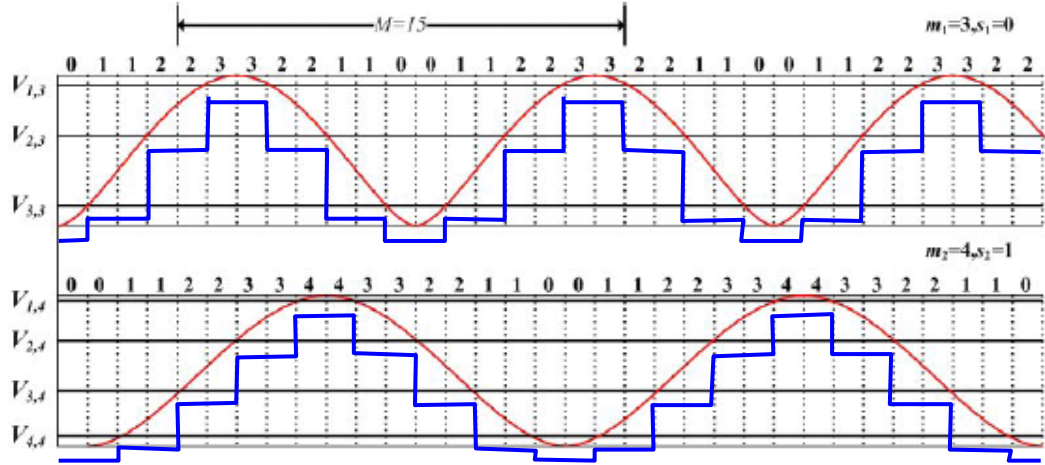


Figure 6. Mapping RSNS folding waveforms to threshold values (After [4]).

h. *Calculate the phase adjustment term for each channel.* The phase adjustment term for each channel maps the center of the dynamic range to the response of the antenna when the signal AOA is at broadside. Referring to Table 1, neither modulus has symmetry about the midpoint of the dynamic range, which is $h=11$. Therefore, a phase adjustment ς is added to Equation (2.4) giving

$$V_{out}(\theta) = \cos(kd \sin \theta + \varsigma) \quad (3.16)$$

When $\theta=0$, $\sin(\theta)=0$, so $V_{out}(\theta=0) = \cos(\varsigma)$. The value of ς is selected so that $V_{out}(\theta=0)$ is encoded to the center bin of the system dynamic range. In the example shown in Table 1, $V_{out}(\theta=0)$ should be encoded into $\varsigma=0$ for m_1 and $\varsigma=3$ for m_2 . Note that the unit for phase adjustment is in radians.

At this point, the relationship between the RSNS digital output and the angle of arrival has been established. Using this relation, we can plot the transfer function of the processor, which is a plot of actual AOA versus the estimated AOA.

2. Resolution of the RSNS Interferometer

Studies [12] have shown that the estimated AOA θ_u' for the u^{th} bin is given as

$$\theta_u' = \sin^{-1} \left(\frac{2u+1}{\hat{M}_\xi} - \frac{1}{\xi} \right) \quad (3.17)$$

and the AOA resolution r_u for the u^{th} bin is given as

$$r_u = \sin^{-1} \left(\frac{2u - \hat{M} + 2}{\hat{M}_\xi} \right) - \sin^{-1} \left(\frac{2u - \hat{M}}{\hat{M}_\xi} \right) \quad (3.18)$$

Note that the resolution changes throughout the FOV.

C. DESIGN EXAMPLE AND EXPERIMENTAL RESULTS

In this section, a two-channel, 6-bit RSNS antenna design originally given in [5] is described to illustrate the design procedures. The schematic diagram shown in Figure 7 is for the design of a 6-bit RSNS-based interferometer using $m_1=8$ ($s_1=0$) and $m_2=17$ ($s_2=1$). Printed circuit dipoles operating at the frequency of 8.0 GHz were used for the antenna elements. In this analog architecture, the thresholds crossings were detected using comparators.

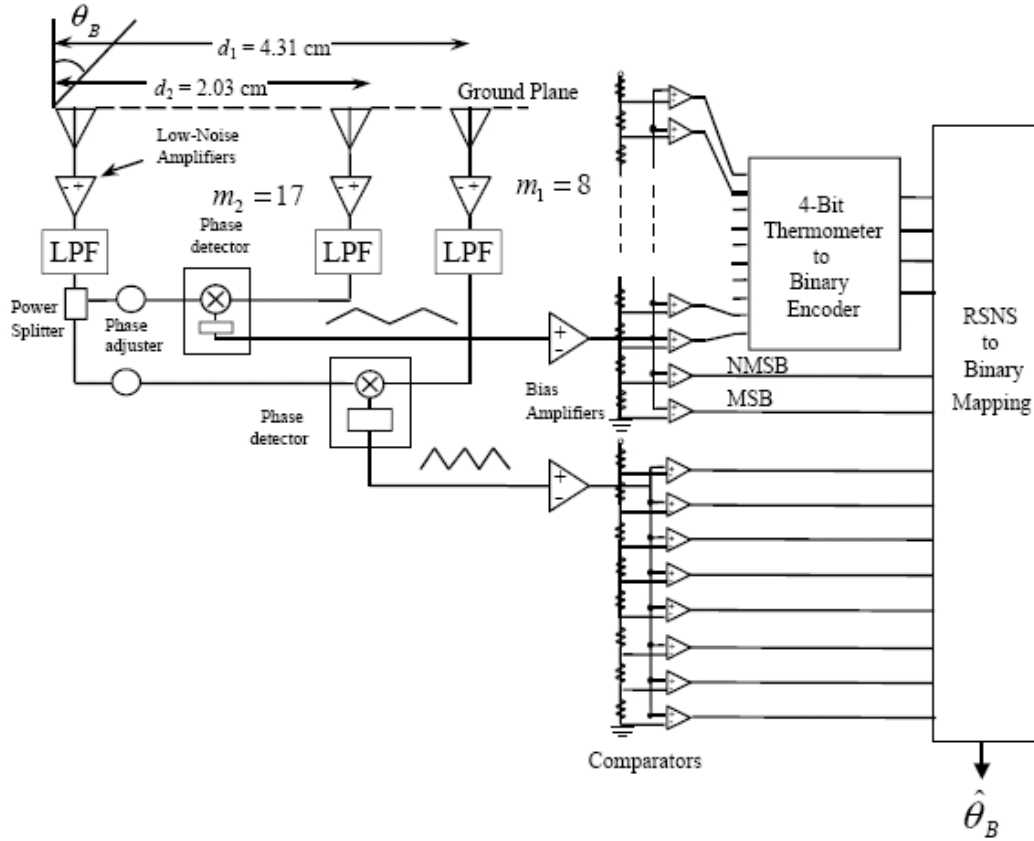


Figure 7. Block diagram of the RSNS-based DF System (From [5]).

1. Design of the DF System

The design of the system is broken down into the steps described in the previous section for the application of RSNS to interferometers.

a. The number of channels required is 2. The number of required antenna elements is 3.

b. *Identify an integer valued modulus for each channel (m_1, m_2).* The chosen moduli are $m_1=8$ and $m_2=17$. This is considered a pairwise relatively prime (PRP) moduli set.

c. *Determine the system dynamic range based on the chosen moduli.* Using the MATLAB search program, the dynamic range is determined to be 64. The RSNS sequence is shown in Table 2.

l	m_1	m_2	n	l	m_1	m_2	n	l	m_1	m_2	n
21	6	10	0	43	5	13	22	65	0	2	44
22	5	10	1	44	6	13	23	66	1	2	45
23	5	11	2	45	6	12	24	67	1	1	46
24	4	11	3	46	7	12	25	68	2	1	47
25	4	12	4	47	7	11	26	69	2	0	48
26	3	12	5	48	8	11	27	70	3	0	49
27	3	13	6	49	8	10	28	71	3	1	50
28	2	13	7	50	7	10	29	72	4	1	51
29	2	14	8	51	7	9	30	73	4	2	52
30	1	14	9	52	6	9	31	74	5	2	53
31	1	15	10	53	6	8	32	75	5	3	54
32	0	15	11	54	5	8	33	76	6	3	55
33	0	16	12	55	5	7	34	77	6	4	56
34	1	16	13	56	4	7	35	78	7	4	57
35	1	17	14	57	4	6	36	79	7	5	58
36	2	17	15	58	3	6	37	80	8	5	59
37	2	16	16	59	3	5	38	81	8	6	60
38	3	16	17	60	2	5	39	82	7	6	61
39	3	15	18	61	2	4	40	83	7	7	62
40	4	15	19	62	1	4	41	84	6	7	63
41	4	14	20	63	1	3	42	85	6	8	

Table 2. RSNS Sequence for $m_1=8$ and $m_2=17$ (From [3]).

d. *Define the number of folds within each modulus.* Applying Equation (3.10), the respective number of folds are calculated to be $n_1=2$ and $n_2=16/17$.

e. *Determine the required antenna spacing for each channel.* The number of folds is simply multiplied by half a wavelength to determine the required distances. In this case, the wavelength is 3.75 cm for frequency of 8 GHz. This results in unscaled distances of $d_1=3.75$ cm and $d_2=1.765$ cm.

f. *Scaling the FOV.* A scaling factor of $\xi = \frac{2}{\sqrt{3}}$ was chosen to re-map the FOV from $\pm 90^\circ$ to $\pm 60^\circ$. The corresponding scaled element spacing, determined by Equation (3.14) are $d'_1=4.33$ cm and $d'_2=2.04$ cm.

g. *Determine the thresholds.* The thresholds are shown in Table 3.

Comparator	Channel m_1	Channel m_2	Comparator	Channel m_1	Channel m_2
1	$\cos(15\pi/16)$	$\cos(33\pi/34)$	10	-----	$\cos(15\pi/34)$
2	$\cos(13\pi/16)$	$\cos(31\pi/34)$	11	-----	$\cos(13\pi/34)$
3	$\cos(11\pi/16)$	$\cos(29\pi/34)$	12	-----	$\cos(11\pi/34)$
4	$\cos(9\pi/16)$	$\cos(27\pi/34)$	13	-----	$\cos(9\pi/34)$
5	$\cos(7\pi/16)$	$\cos(25\pi/34)$	14	-----	$\cos(7\pi/34)$
6	$\cos(5\pi/16)$	$\cos(23\pi/34)$	15	-----	$\cos(5\pi/34)$
7	$\cos(3\pi/16)$	$\cos(21\pi/34)$	16	-----	$\cos(3\pi/34)$
8	$\cos(1\pi/16)$	$\cos(19\pi/34)$	17	-----	$\cos(1\pi/34)$
9	-----	$\cos(17\pi/34)$	-----	-----	-----

Table 3. Threshold Values for Moduli set {8 17} (From [5]).

h. *Calculate the phase adjustment term for each channel.* A phase adjuster ζ_i for each channel is calculated using Equation (3.16). The normalized voltage output for channel m_1 after adding a phase adjustment is given as

$$V_{out1}(\theta) = \cos\left(kd_1 \sin \theta + \frac{\pi}{4}\right) \quad (3.19)$$

and for channel m_2 ,

$$V_{out2}(\theta) = \cos\left(kd_2 \sin \theta + \frac{\pi}{2}\right) \quad (3.20)$$

Figure 8 depicts the folding output waveforms from Equations (3.19) and (3.20). The corresponding quantized folding output waveforms are plotted in Figure 9.

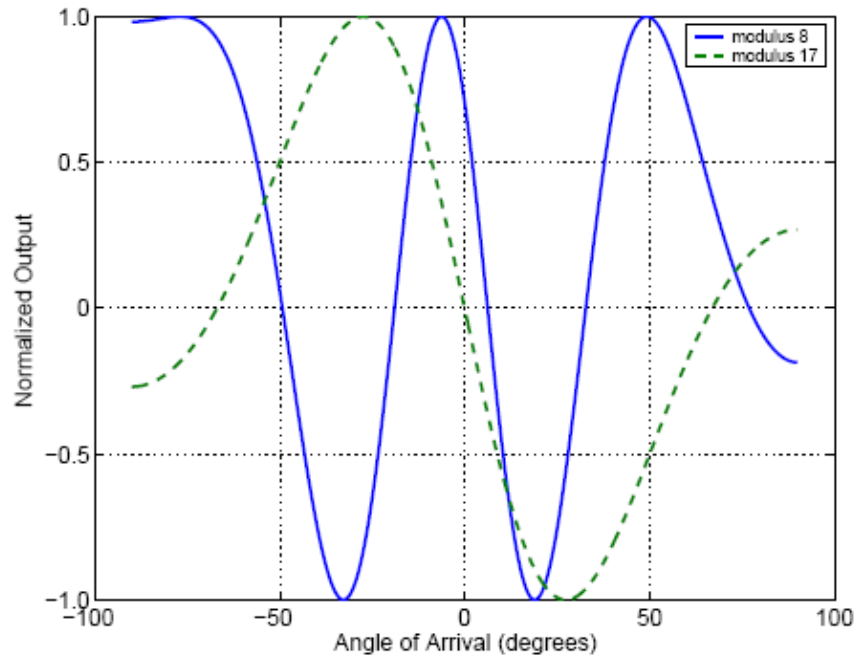


Figure 8. Folding Output Waveforms with Phase Adjustment (From [7]).

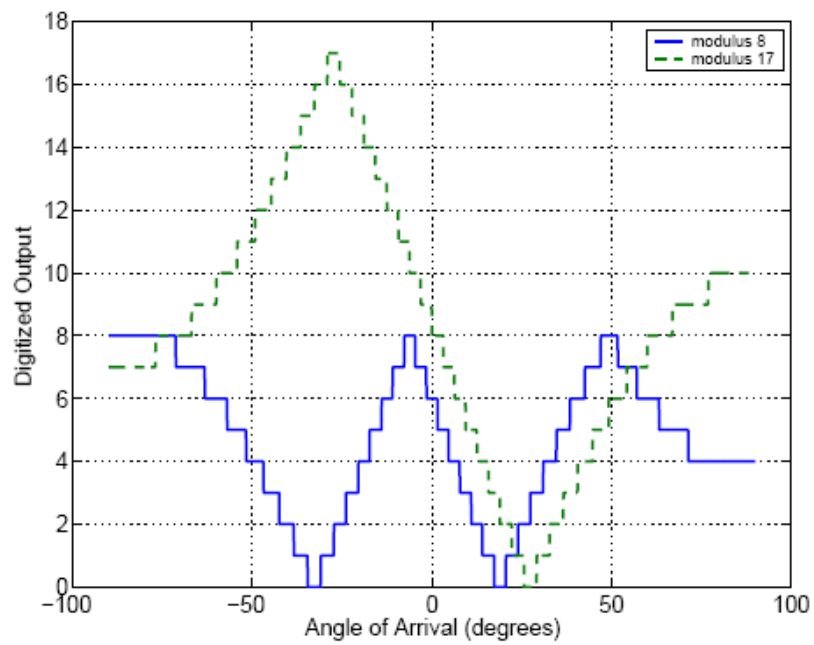


Figure 9. Phase Adjusted Folding Waveforms after Comparators (From [7]).

Finally, by combining the information in Table 2 and Figure 9, and using Equation (3.17), we can obtain a plot of estimated AOA versus true AOA as shown in Figure 10.

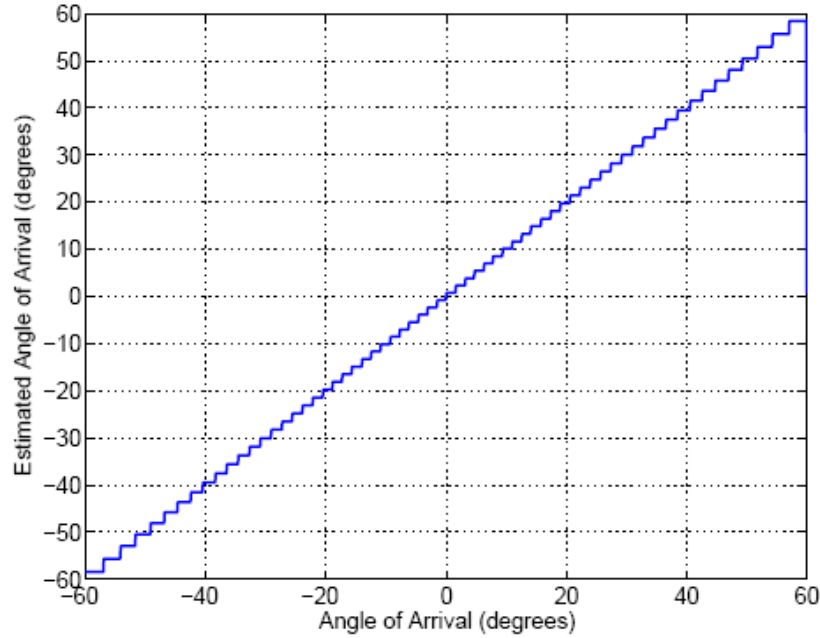


Figure 10. Transfer Function, the Estimated AOA versus Actual AOA (From [7]).

2. Experimental Results and Analysis

A prototype circuit based on Figure 7 was built and tested [5]. The measured AOA versus true AOA is shown in Figure 11.

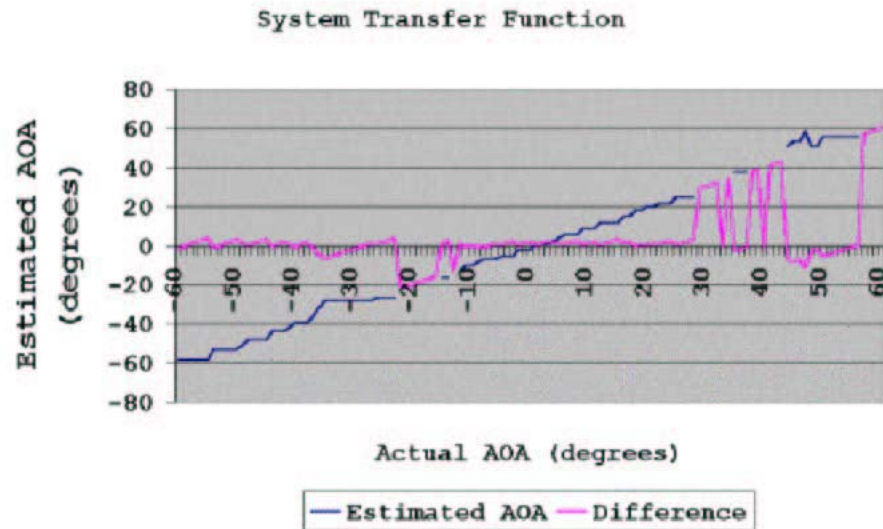


Figure 11. Measured RSNS Transfer Function (From [5]).

The experimental results exhibit the basic features of the simulated (ideal) transfer function shown in Figure 10. However, the performance, while promising, contains large fading regions which are in part due to the analog components that were used. These issues have been discussed in [3-5, 7]. In [7], an error analysis was performed on each fundamental parameter, including antenna spacing and phase adjustment errors, to show how the SNR affects the performance of the transfer function.

D. SUMMARY

This chapter has covered the principles of designing a RSNS based DF system. A design example and the results of previous work were reviewed. In the next two chapters, the design and implementation of a RSNS-based DF demonstration system is described.

IV. DESIGN OF RSNS-BASED DF DEMONSTRATION ARRAY – DETERMINING RSNS PARAMETERS

This chapter describes the design considerations and RSNS parameters used for implementation of the demonstration array. The objective was to build a high-resolution RSNS-based DF demonstration array employing digital architecture.

To achieve this goal, it's necessary to determine the key design parameters, such as the signal frequency on which DF testing will be conducted, as well as the RSNS parameters, which determine the array size and antenna element spacing. We shall first present how the RSNS parameters were determined for the demonstration array before discussing the practical implementation and hardware used to assemble the array (next chapter).

A. DETERMINING RSNS PARAMETERS

Using the steps laid out in section C of Chapter 3, the key parameters of the RSNS DF system were decided in consultation with the thesis advisors.

1. *Determine N , number of channels required.* A 3-channel system was decided upon, as a previous implementation with a two-channel analog system [5] had been tested. A total of four antenna elements would be required for the 3-channel system.

2. *Identify an integer valued modulus for each channel ($m_1, m_2 \dots m_i$).* In order to achieve a high resolution system, a PRP moduli set was used. Steps 2 through 5 were carried out to obtain options for consideration. The moduli set of {7 15 29} was decided upon, as it provided the dual benefits of high resolution and a short antenna baseline requirement.

3. *Determine the system dynamic range based on the chosen moduli.* The dynamic ranges for each of the moduli set under consideration were

determined by means of the MATLAB-based RSNS search program. For our chosen moduli set, the dynamic range was determined to be $\hat{M} = 444$.

4. *Define the number of folds within each modulus.* This is calculated by dividing the dynamic range by the period of the each modulus. The number of folds within each modulus were determined to be

$$n_1 = 10.5952,$$

$$n_2 = 4.9444, \text{ and}$$

$$n_3 = 2.5575$$

5. *Determine the required antenna spacing.* The required antenna spacing is determined by multiplying the number of folds by half the wavelength of the signal frequency of interest. Based on the readily available RF components for building the demonstration array, a signal frequency of 2.4 GHz was selected. This equates to a wavelength of 12.5 cm. The required antenna element spacing from the reference antenna are:

$$d_1 = 66.22 \text{ cm},$$

$$d_2 = 30.9 \text{ cm}, \text{ and}$$

$$d_3 = 15.98 \text{ cm}$$

6. *Re-mapping the FOV.* Given high resolution available from the chosen PRP moduli, the FOV was not scaled and the scaling factor used for the RSNS algorithm was unity.

7. *Determine the thresholds.* For each channel, there would be corresponding number of thresholds matching the modulus number. The chosen moduli set of {7 15 29} therefore yields a corresponding number of thresholds as shown in Table 4.

Threshold #	Modulus 1 : 7	Modulus 2 : 15	Modulus 3 : 29
1.	-0.9749	-0.9945	-0.9985
2.	-0.7818	-0.9511	-0.9868
3.	-0.4339	-0.8660	-0.9635
4.	0	-0.7431	-0.9290
5.	0.4339	-0.5878	-0.8835
6.	0.7818	-0.4067	-0.8277
7.	0.9749	-0.2079	-0.7622
8.	-	0	-0.6877
9.	-	0.2079	-0.6052
10.	-	0.4067	-0.5156
11.	-	0.5878	-0.4199
12.	-	0.7431	-0.3193
13.	-	0.8660	-0.2150
14.	-	0.9511	-0.1081
15.	-	0.9945	0
16.	-	-	0.1081
17.	-	-	0.2150
18.	-	-	0.3193
19.	-	-	0.4199
20.	-	-	0.5156
21.	-	-	0.6052
22.	-	-	0.6877
23.	-	-	0.7622
24.	-	-	0.8277
25.	-	-	0.8835
26.	-	-	0.9290
27.	-	-	0.9635
28.	-	-	0.9868
29.	-	-	0.9985

Table 4. Threshold Values for Demonstration Array.

8. *Calculate the phase adjustment term for each channel.* The phase adjustment terms for the respective channels were similarly determined by means of a MATLAB-based search program developed in [7]. The required phase adjustments are shown in Table 5.

	Phase Adjustment Term
Channel 1	-1.4960 radians
Channel 2	0.0698 radians
Channel 3	0.8666 radians

Table 5. Phase Adjustment Terms for Demonstration Array.

B. STIMULATION RESULTS FOR DF ARRAY USING MODULI {7 15 29}

With the key RSNS design parameters determined, the transfer function, which shows the actual AOA versus the estimated AOA, is plotted in Figures 12 to 14.

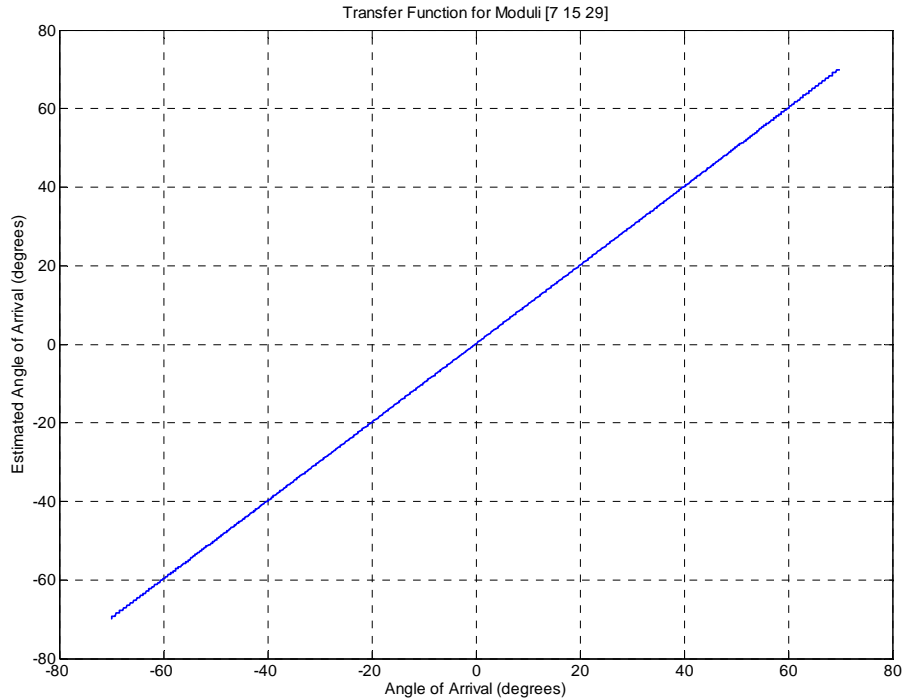


Figure 12. Transfer Function for Demonstration Array using Moduli {7 15 29}.

Examining the transfer function in Figure 12, it looks like a smooth straight line due to the high resolution; 444 bins over the unscaled FOV of -90 to 90 degrees. In Figure 13, we examine the transfer characteristics in greater detail when the AOA is in the vicinity of broadside.

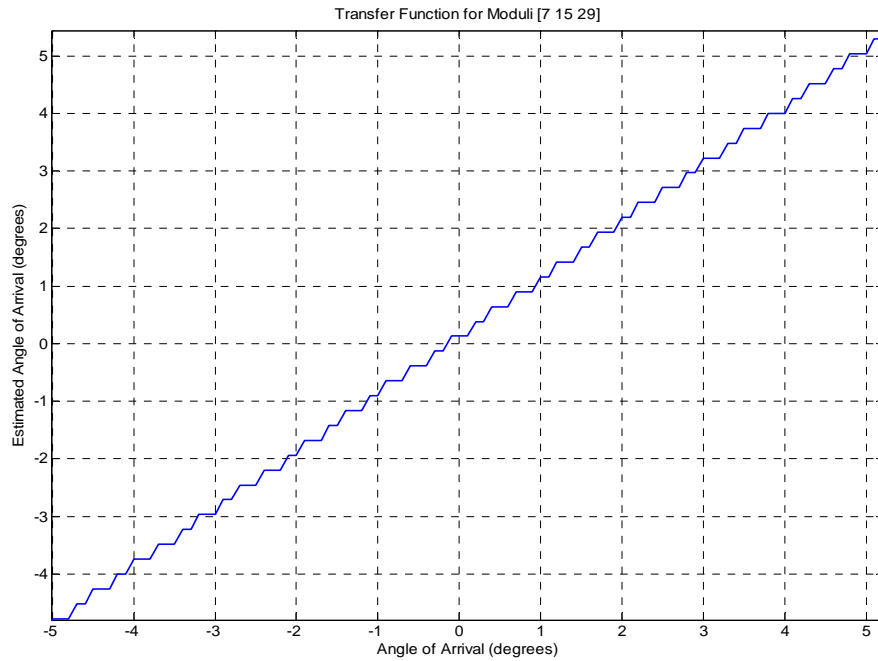


Figure 13. Transfer Function Near Broadside.

In Figure 13, it is evident that the transfer function maps the estimated AOA of the signal in discrete increments, producing a stair-case like function. This effect is due to the discrete nature of the mapping of the RSNS folding waveforms and coding by means of detecting threshold crossings. In Figure 14, we examine the transfer function at high AOA angles.

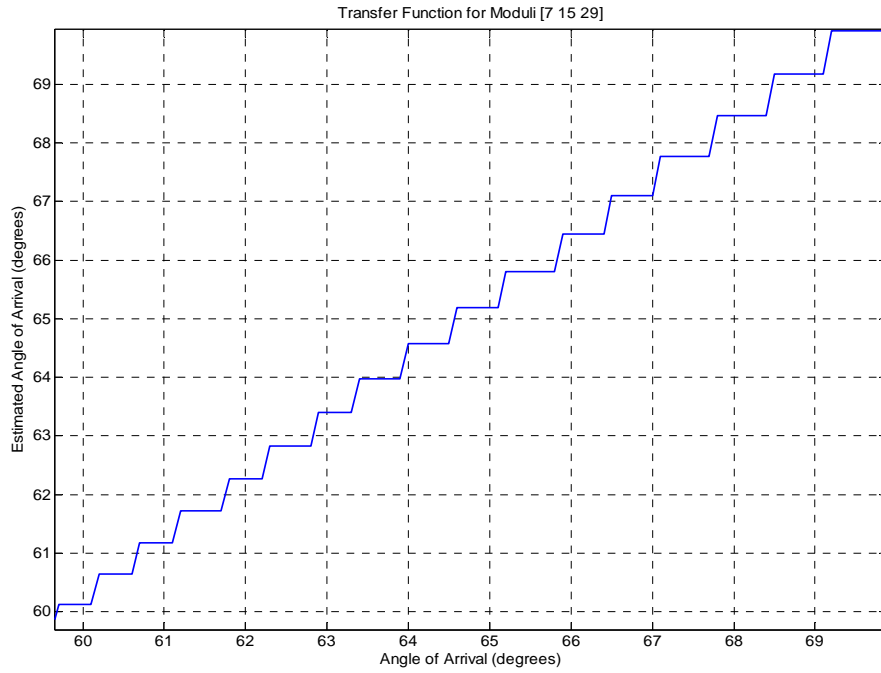


Figure 14. Transfer Function at High AOA Angles.

Comparing Figure 13 with Figure 14, the discrete behavior is present in both plots but more pronounced as we increase the signal AOA. The resolution of the DF system increases as we increase the AOA angle and more than doubles at 65 degrees. The resolution can be determined by Equation (3.18) and it conforms to an arc-sine relationship. Examining the simulated quantization error shown in Figure 15 through 17, it is evident that the errors increase correspondingly with signal AOA.

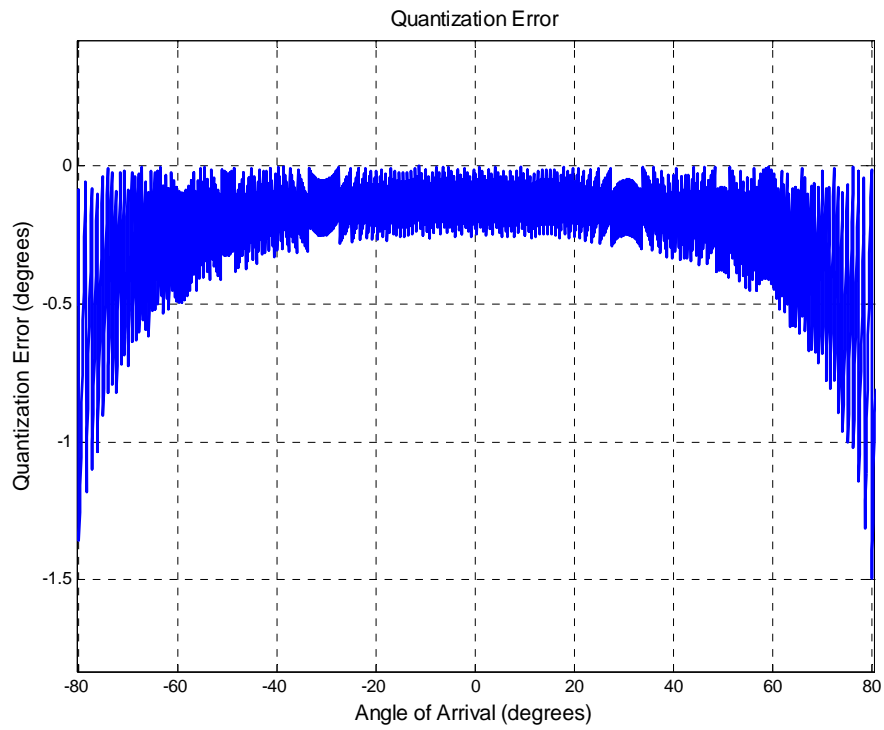


Figure 15. Quantization Error for Demonstration Array.

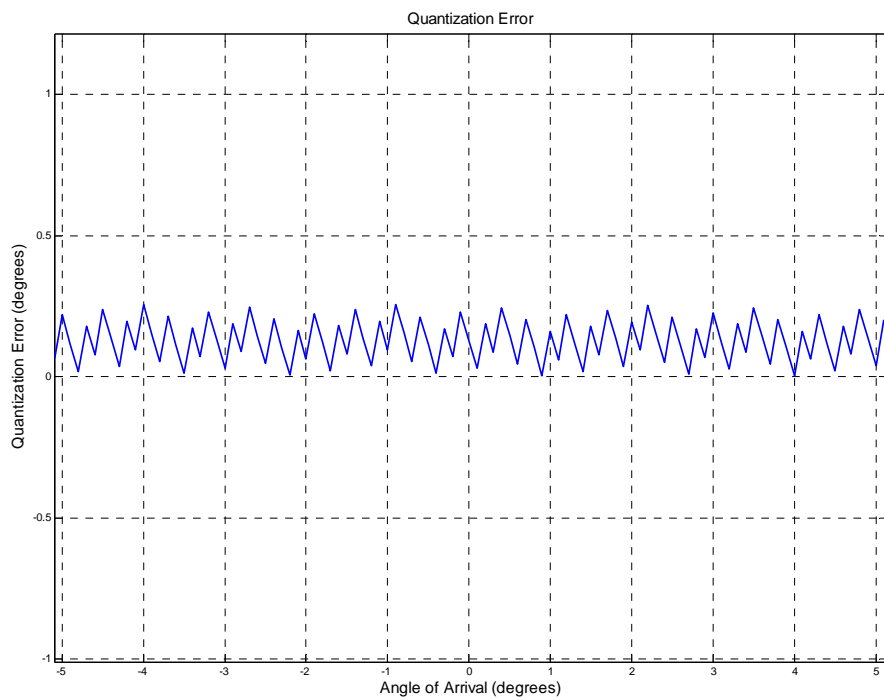


Figure 16. Quantization Error Near Broadside.

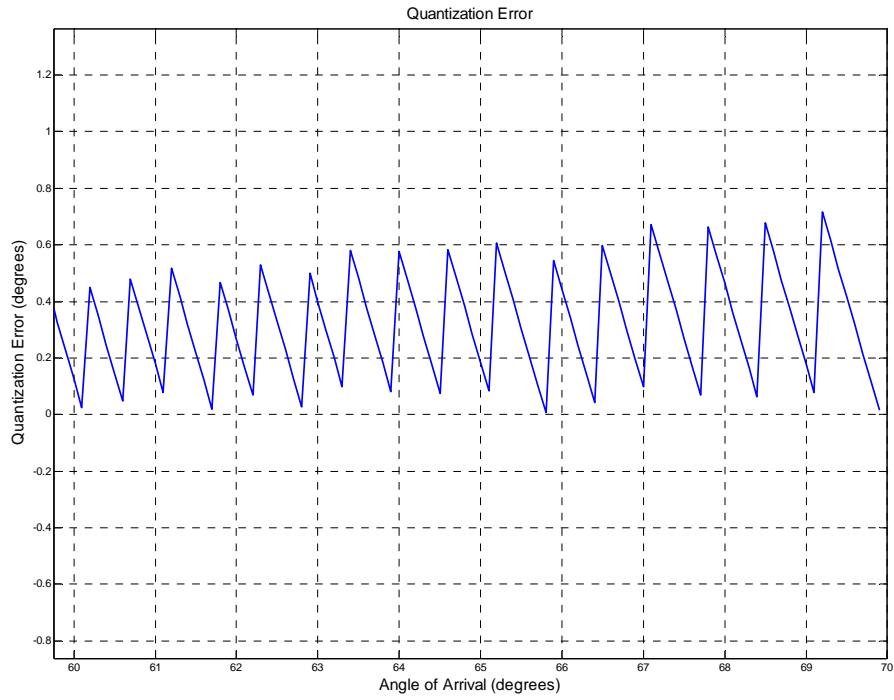


Figure 17. Quantization Error at High AOA Angles.

C. SUMMARY

The key RSNS design parameters for the demonstration system are summarized below:

Operating Frequency = 2.4 GHz
Wavelength = 12.5 cm
Half wavelength = 6.25 cm

	m_i values	Folds in each m_i	Dist btw elements (cm)
m_1	7	10.5	66.22
m_2	15	4.93	30.9
m_3	29	2.55	15.98

Dynamic Range = 444
Resolution at broadside = 0.258°
Resolution at 60° AOA = 1.311°

With the RSNS design parameters determined and simulations conducted, we move on to build the demonstration system. The next chapter covers the hardware and control software of the demonstration system.

THIS PAGE INTENTIONALLY LEFT BLANK

V. DESIGN OF RSNS-BASED DF DEMONSTRATION ARRAY – HARDWARE AND SOFTWARE IMPLEMENTATION

A significant portion of the initial work on the characterization of the hardware as well as the initial LabView programs for calibration of the demodulator board were spear-headed by Gert Burgstaller [13] and Levant Gezer [14]; two students who graduated in September 2006. We were working with several identical hardware components and aspects of the LabView software. Their initial work contributed significantly in overcoming a steep learning curve on building the demonstration array and programming LabView for signal sampling and processing.

Gert Burgstaller conducted a detailed analysis and characterization of the hardware components [13]. A number of diagrams and pictures in this chapter are referenced to his thesis.

Levant Gezer wrote a LabView program to control ADCs for sampling I/Q data from eight demodulators [14]. The LabView program used for controlling the demonstration system is based heavily on his program, modified and scaled down for controlling four ADC for our application.

A. HARDWARE DESIGN

The electronics hardware used to build the demonstration array is from COTS sources. A number of parts such as the variable power supply and RF shielding were built by Bob Broadston, Lab director of the Microwave lab. Other parts such as the antenna array, mounting blocks and power cables were built with his assistance. The block diagram in Figure 18 shows the hardware used in the demonstration array.

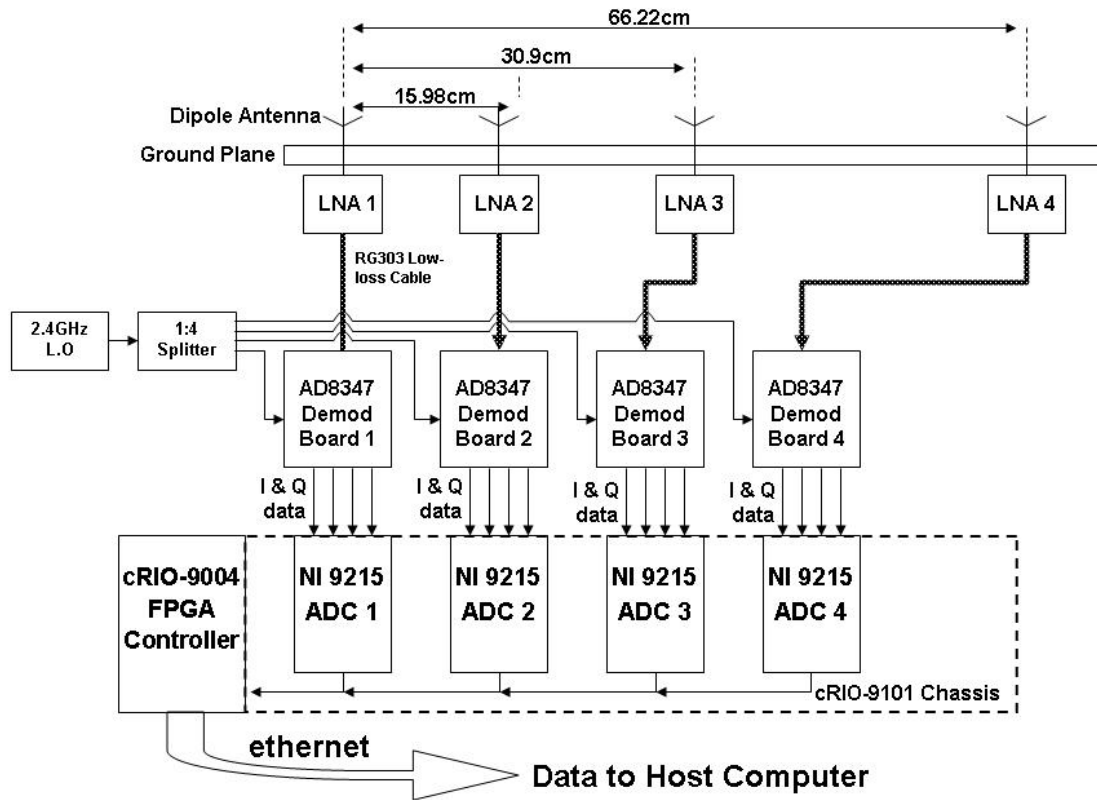


Figure 18. Hardware Block Diagram of Demonstration Array.

After the I/Q data has been sampled and quantized from the demodulator boards, it is fed to the host computer through a Ethernet connection for signal processing.

B. OVERVIEW OF HARDWARE COMPONENTS

A majority of the key hardware components used in the demonstration array are National Instruments (NI) modular systems. Along with the hardware like the ADC and controller modules, LabView Version 8.0 is the main software application that is used for both controlling the hardware and the implementation of the RSNS algorithm through embedded MATLAB scripts within the LabView program.

The key components in the demonstration array are described in the following section in order of signal flow, starting with the antenna elements and ending with the Ethernet connection to the host computer. The key specifications and description of the hardware components are covered in this section.

Component	Quantity	Remarks
Dipole Antennas	4	From previous thesis project
Ground Plane	1	DIY board with copper foil
LNA-2700	4	Low noise amplifier
RG303 cables	4	New from Pasterneck, Lower losses compared to RG58 for RF signals
AD8347-EVAL	4	Demodulator boards from Analog Devices
VCO2400	1	New from RF Bay Inc, not used due to frequency drifts
Power Splitter	1	Used to split LO signal for demodulator boards
RG58 cable	16	4 for each demodulator board
NI-9215 ADC	4	Analog to Digital conversion for I&Q signals
NI cRIO-9101	1	4 slot reconfigurable embedded chassis to house the NI-9215 ADCs
NI cRIO-9004	1	FPGA real time controller
Power supply unit	1	Provides 5V and 12V outputs
Variable Voltage	1	DIY to provide 0.38V for demod boards
Ethernet cable	1	To link up to host computer

Table 6. List of Hardware Components.

1. Dipole Antenna Element

The antenna array utilizes printed circuit dipole antennas from a previous thesis project. The dipole antennas were designed with a nominal operating frequency of 2.4 GHz and a return loss of over 15 dB. A dipole mounted in a ground plane and one standing alone is shown in Figure 19. This setup with a

single element was used for testing by Gert Burgstaller in the anechoic chamber to determine the dipole antenna pattern.



Figure 19. Two Dipole Elements, One Mounted in a Ground Plane (From [13]).

The element gain, G_{dipole} , was measured in the chamber using a comparative method. The measured element patterns for the printed dipole antenna mounted in a ground plane at 2.4 GHz are displayed in Figure 20.

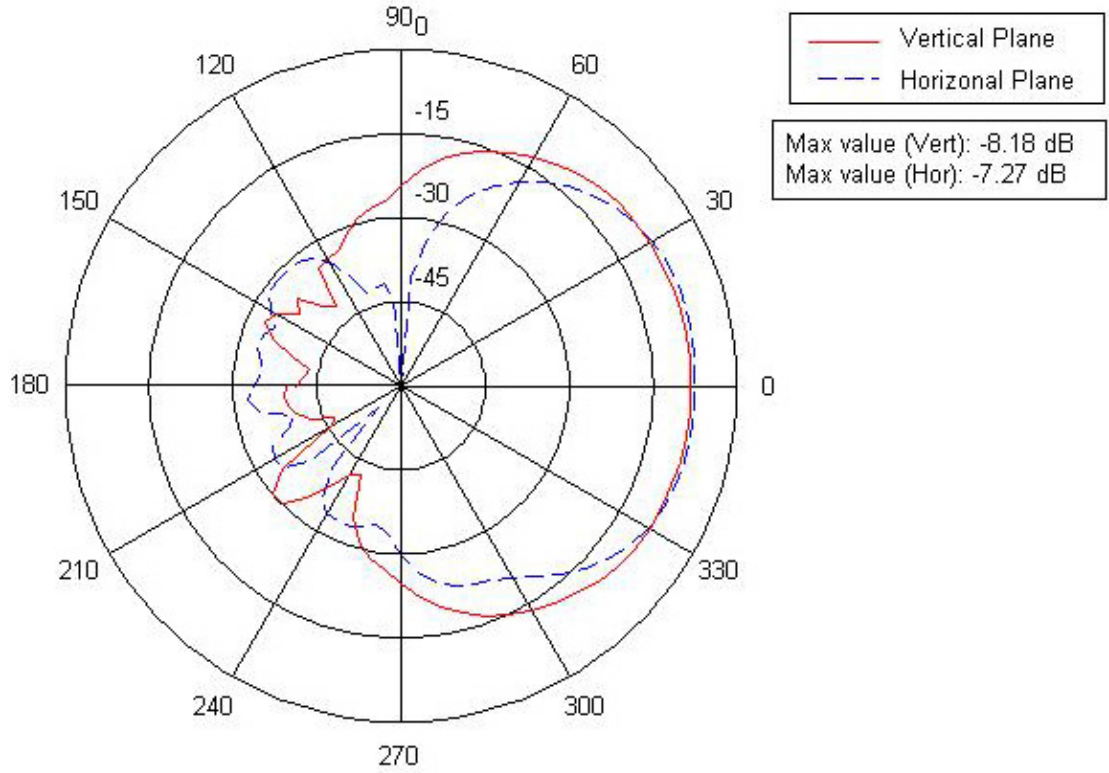


Figure 20. Dipole element pattern measurement measured at 2.40 GHz (From [12]).

The average maximum pattern value for the received power for the two polarizations is

$$\frac{(-8.18) + (-7.27)}{2} = -7.72 \text{ dB.} \quad (5.2)$$

The gain of the printed circuit dipole antenna mounted in the ground plane compares to the reference measurement by

$$2.85 - (-7.72) = 17.12 - G_{dipole}, \quad (5.3)$$

and finally the dipole element gain is established at

$$G_{dipole} = 17.12 - 2.85 - 7.72 = 6.55 \text{ dB}$$

The 3dB beamwidth of the elements at 2.4 GHz is approximately 65 degrees.

2. Ground Plane

The ground plane was built by using adhesive glue to bond copper foil coatings to a wooden chip board. Measuring 32 inches by 12 inches, it was designed to have a ground plane spacing in excess of half wavelength from antenna elements at the operating frequency of 2.4 GHz. The required position of antenna slots were measured as precisely as possible and slots were carefully cut for insertion of the dipole antenna elements. Although extreme care was taken during the entire process, distance errors (horizontal) as well as vertical alignment between the elements exists as the slots and mounting of antenna elements were made by hand using common household tools.

3. Low Noise Amplifiers (LNA-2700)

The low-noise amplifier was acquired from RF Bay Inc and is shown in Figure 21. Model LNA-2700 was chosen as it suited our needs in terms of size, specifications and its price to performance as shown in Table 7.



Figure 21. Low-Noise amplifier LNA-2700 from RF Bay, Inc.

Parameter	Specification	Unit	Comments
Frequency Range	2.2 – 2.7	GHz	
Gain	23	dB	For operations at 2.4 GHz
Noise Figure	+1.7	dB	For operations at 2.4 GHz
RF Input Power	+13	dBm	Absolute Maximum Rating

Table 7. LNA-2700 Specifications (From [15]).

The verification of the LNAs in terms of its S21 parameters (log and phase response) were conducted on the vector network analyzer (VNA) in the Microwave Lab.

LNA#	Gain (dB)	Phase(degrees)	Phase Relative to LNA 1 (reference)
1	22.8	85.42	-
2	24.86	53.35	-32.07
3	23.02	48.9	-36.52
4	24.65	57.12	-28.30

Table 8. Gain and Response of LNAs.

We observe from Table 8 that the gains of all four LNAs are in-line with the specified 23 dB gain from the manufacturer. Note that the output phase of each LNA is different although the same settings and phase were used during testing. In an analog implementation, these errors would need to be eliminated by means of a phase shifter, connected in-line with each antenna element after the RG-303 cable. The analog calibration would be tedious and likely to be erroneous to a few degrees. In the digital architecture, the phase errors from the antenna, LNA, RG-303 and demodulator response, are easily eliminated in software during the signal processing stage in LabView.

4. RG-303 Cables

The RG-303 cables, 2.5 ft in length, were purchased from Pasternack Enterprises. The cables were not ordered to be phase-matched as these errors can be eliminated during the signal processing stage in LabView.

Manufactured with a silver covered copper clad steel and shielded with silver covered copper, these cables were selected for its relatively low loss at our selected operating frequency of 2.4 GHz. The specifications state a loss of 13 dB per 100 ft at 1 GHz and 39 dB per 100ft at 5 GHz. Interpolated, this gives an approximated loss of 0.3 dB for the 2.5 ft cable .

The cables were tested for losses and phase response on the VNA. Of the four initial cables tested, the second cable was tested to be faulty, with a significantly higher loss of -3.85dB and a phase response which did not match its length. This cable was replaced. The measured cable parameters are shown in Table 9.

RG-303 Cable #	Losses (dB)	Phase(degrees)
1	-0.622	-153.64
2*	-0.65	-153.53
3	-0.662	-150.14
4	-0.625	-153.2

2nd Cable was tested defective and replaced

Table 9. Gain and Phase Response of RG-303 Cables.

5. Demodulator Boards (AD8347-EVAL)

The technique of quadrature demodulation is first explained in this section before the characteristics of the AD8347 demodulator boards [16] are described.

Bandpass signals can be expressed as

$$x_{band}(t) = x_I \cos(\omega_c t) - x_Q \sin(\omega_c t) \quad (5.4)$$

where x_i is defined as the *in-phase* component and x_q is defined as the *quadrature* component. Decomposing a signal into its in-phase and quadrature components acts to preserve the phasor's complete information.

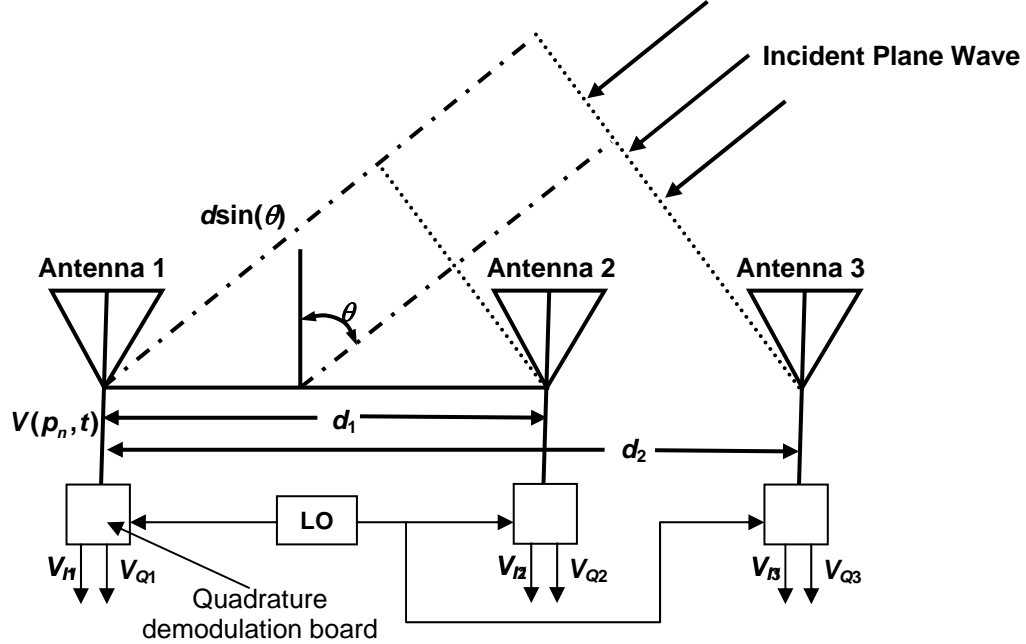


Figure 22. Quadrature Type Demodulation of 2-Channel Interferometer (After [7]).

For the interferometer shown in Figure 22, the output of the antenna elements can be expressed as

$$V(p_n, t) = \text{Re} \{ A(p_n) e^{j(\omega_c t)} \} \quad (5.5)$$

where $n=1,2,3$ represents the antenna element index $A(p_n)$ in the polarization dependent amplitude and

$$A(p_n) = |A(p_n)| e^{j\phi(p_n)} = A_I(p_n) + jA_Q(p_n) \quad (5.6)$$

The outputs from the antenna elements are passed through the quadrature demodulation boards, which are configured as shown in Figure 23.

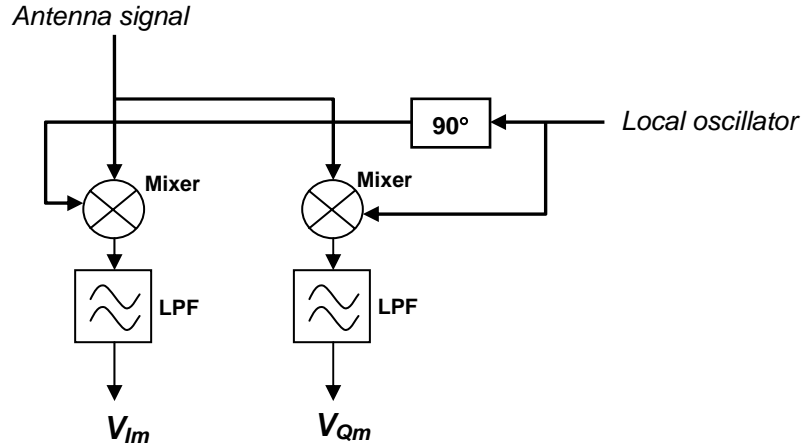


Figure 23. Basic Quadrature Demodulation Processing (After [7]).

The local oscillator (LO) provides a pure tone signal at the antenna signal frequency. The LO_I signal ($V_{LOI} = \cos(\omega_c t)$) is passed through a 90 degree phase shift to obtain the quadrature LO_Q signal.

$$V_{LOQ} = \cos(\omega_c t + \pi/2) = -\sin(\omega_c t) \quad (5.7)$$

The antenna signal is fed to the respective mixers to obtain the in-phase and quadrature terms

$$\begin{aligned} V_I(p_n, t) &= V(p_n, t) \cos(\omega_c t) \\ &= \frac{1}{2} A_I(p_n) + \frac{1}{2} [A_I(p_n) \cos(2\omega_c t) - A_Q(p_n) \sin(2\omega_c t)] \end{aligned} \quad (5.8)$$

$$\begin{aligned} V_Q(p_n, t) &= -V(p_n, t) \sin(\omega_c t) \\ &= -\frac{1}{2} [A_I(p_n) \sin(2\omega_c t) + A_Q(p_n) \cos(2\omega_c t)] + \frac{1}{2} A_Q(p_n) \end{aligned} \quad (5.9)$$

After filtering with a low-pass filter (LPF), we obtain the baseband terms

$$V_I(p_n) = \frac{1}{2} A_I(p_n) = \frac{1}{2} |A(p_n)| \cos(\phi(p_n)) \quad (5.10)$$

$$V_Q(p_n) = \frac{1}{2} A_Q(p_n) = \frac{1}{2} |A(p_n)| \sin(\phi(p_n)) \quad (5.11)$$

For a plane wave $|A(p_n)|$ is a constant and therefore, we can normalize Equations (5.10) and (5.11) to obtain the expressions this line should be at margin

$$V_{In} = V_I(p_n) = \cos(\phi(p_n)) \quad (5.12)$$

$$V_{Qn} = V_Q(p_n) = \sin(\phi(p_n)) \quad (5.13)$$

Equations (5.12) and (5.13) are referred to as the ***in-phase*** and ***quadrature*** terms of the signal received by antenna element n . To obtain the phase differential between antenna elements 1 and 2, same here

$$\Delta\phi_{12} = \phi(p_1) - \phi(p_2) = \arctan\left(\frac{V_{Q1}}{V_{I1}}\right) - \arctan\left(\frac{V_{Q2}}{V_{I2}}\right) = kd_1 \sin \theta \quad (5.14)$$

where d_1 is the distance between antenna elements 1 and 2.

The output I and Q voltages are digitized using an Analog-to-Digital Converter (ADC) for subsequent signal processing. We obtain the equivalent of the analog normalized output voltage in Equation (2.4) by taking the cosine of the phase differential in Equation (5.14) same

$$V_{12}(\phi) = \cos(kd_1 \sin(\theta)) = \cos(\Delta\phi_{12}) \quad (5.15)$$

The AD8347 demodulator board as shown in Figure 24 was originally designed for communication applications, likely for use in a quadrature phase shift keying technique. When operating in automatic gain control (AGC) mode, the I/Q-channel differential outputs mapped the phase response on the main axes instead of being distributed uniformly around the I/Q circle as the input signal phase is altered.

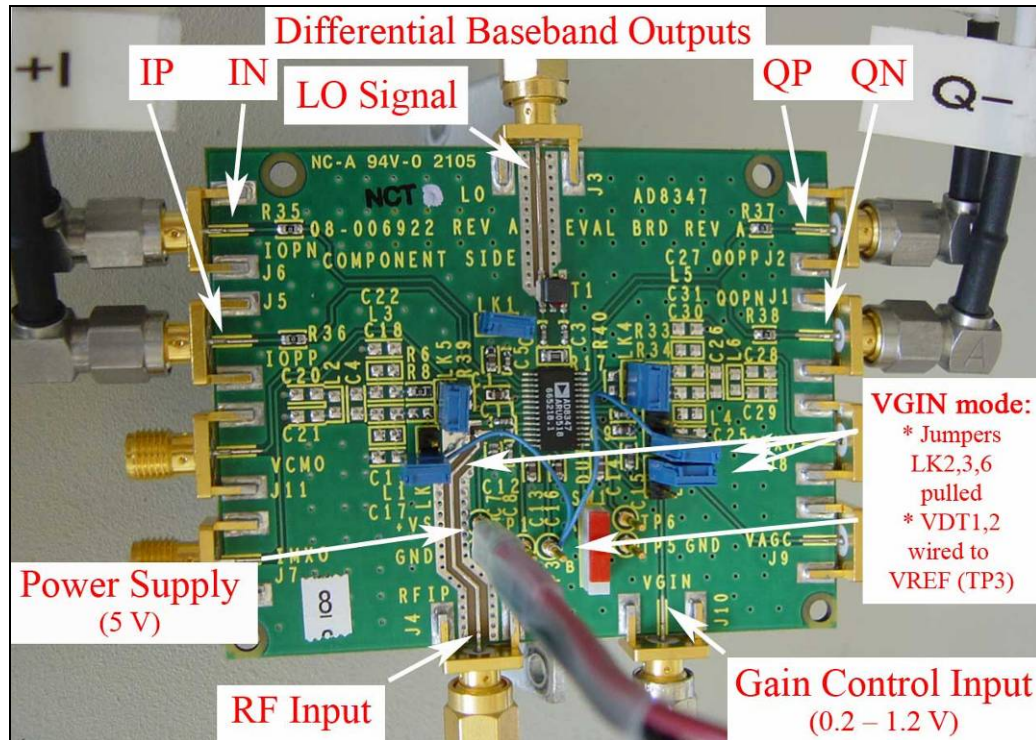


Figure 24. AD8347EVAL wiring connections and mode settings (From [13]).

In order to achieve a linear phase response, the demodulator was re-wired for operation in 'VGIN mode', where the gain of the system was controlled by means of an input voltage at the VGIN pin. The modification for operating the demodulator in VGIN mode was proposed and designed by Bob Broadston. The modifications made to the board are listed in Table 10.

Parameter	Measures taken	Comments
Jumper LK2	Opened	Disconnects I-channel baseband mixer (IMXO, pin 8) from device on-board detector input (VDT2, pin 18)
Jumper LK3	Opened	Disconnects automatic gain control voltage output (VAGC, pin 19) from the demodulator gain control voltage input (VGIN, pin 17)
Jumper LK6	Opened	Disconnects Q-channel baseband mixer (QMXO, pin 22) from on-board detector input (VDT1, pin 20)
VDT1&2	Wired	Connects both detector input voltages (pin 20 & 18) to the chip reference voltage output of 1.0 V (VREF, pin 14)

Table 10. Modifications Made to Operate the AD8347 Demodulator in VGIN Mode (After [13]).

The initial setup, LabView program, excel and MATLAB scripts used for the characterization of the demodulators were developed by Gert Burgstaller and Levent Gezer. The setup and developments during the initial tests are comprehensively covered in [13]. As a direct result of their tests, an optimal VGIN voltage of 0.38 volts was found to produce a good compromise between linear phase response and magnitude of the I/Q circles. One setback of operations in VGIN mode is the occurrence of direct current (DC) offsets that are unique for each demodulator board.

Figure 25(a) displays phase data for the ten AD8347 demodulator boards that were characterized by Burgstaller and Levent for use in their respective projects. Figure 25(b) shows the same I/Q data centered at origin by subtracting the circle center values.

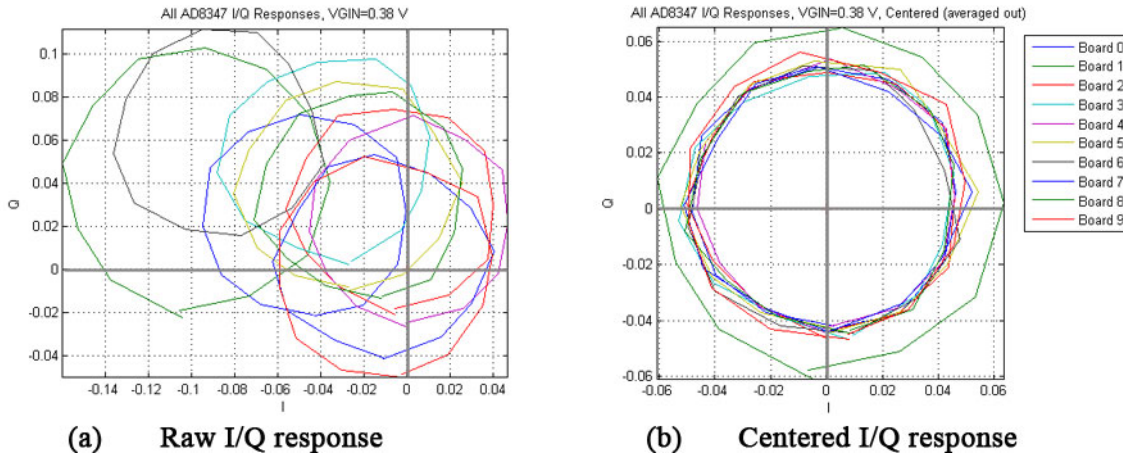


Figure 25. Plotted AD8347 Demodulator Phase Characteristics (From [12]).

For our demonstration array, four demodulator boards were re-wired and modified for operations in VGIN mode. Using a VGIN of 0.38 volts, the boards were characterized. The initial calibration conducted provided reasonably good results and the results from two additional calibration runs were in close agreement. Table 11 tabulates the phase response of these boards and the final calibration offsets used for the demonstration array.

Board No.	Diameter $\Delta I/\Delta Q$ [mV]	Off-center I_0/Q_0 [mV]	Measurement No. & Date
1	ΔI 85.7 ΔQ 86.9	I -1.3231 Q +50.2538	02-Sep-06
2	ΔI 97.6 ΔQ 99.1	I -24.6154 Q +48.5154	02-Sep-06
3	ΔI 84.4 ΔQ 82.2	I -36.8769 Q +47.5154	02-Sep-06
4	ΔI 95 ΔQ 96.9	I -49.3615 Q +51.6308	02-Sep-06

Table 11. AD8347 Phase Response.

6. Power Splitter

A 1:4 power splitter is used to split a single local oscillator signal into four outputs which are supplied to the four demodulator boards. During the initial measurements, the relative phase difference was in the region of 2 to 4 degrees, but this was found to have resulted from uneven tightening of the SMA joints, an issue resolved by using a fixed torque wrench to ensure a uniform tightness across all joints. The parameters of the power splitter are shown in Table 12.

Channel #	Losses (dB)	Phase(degrees)	Relative Phase
1	-6.5	-46.33	-
2	-6.47	-45.9	+0.405
3	-6.48	-46.72	-0.4
4	-6.5	-47.04	-0.67

Table 12. Parameters of Power Splitter.

7. RG-58 Cable

The RG-58 cables, 2.5 ft in length, were purchased from same manufacturer as the RG-303 cables; Pasterneck Enterprises. These cables connect the differential outputs from the demodulator board to the NI-9215 ADCs. There is no requirement for the use of low-loss or phase-matched cables as the differential I/Q outputs from the demodulator are in DC voltage. For each demodulator board, four RG-58 cables are used.

8. National Instrument Modules

A total of three types of NI modules are used in the demonstration array, including 4 ADCs, a chassis to house the ADCs, and the main controller, which is a field programmable gate array (FPGA) system as shown in Figure 26.

- NI cRIO-9004 Real-Time Controller with 64 MB DRAM, 512 MB CompactFlash,
- NI cRIO-9101 4-Slot, 3 M Gate CompactRIO Reconfigurable Embedded Chassis, and

- NI-9215 4-Channel, 100 kS/s, 16-bit, ± 10 V Simultaneous Sampling Analog Input Module.



Figure 26. NI Modular Systems Used for Demonstration Array
(From [17-19]).

In order to operate, control and communicate to the FPGA devices, LabView 8.0, a software program developed by National Instruments, was used. While it is possible to load the entire control and signal processing program into the FPGA, a host virtual instrument (VI) program running off a laptop computer was used for the signal processing. Implementing the signal processing on the host computer allows for changes to be made to the program or algorithm without having to compile and download the new program to the FPGA, a process that takes approximately 30 minutes for the program used for the demonstration array. In our setup, the FPGA program simply initializes the modules, calibrates them, and transfers the digitized I/Q data from the demodulator boards to the host computer for signal processing.

Version 8 of the software (see Figure 27) includes the capability to embed MATLAB scripts directly into the LabView program. This capability is an important aspect of the software as it allows for real-time complex signal processing and algorithms to be implemented in MATLAB code instead of having to process the data off-line.

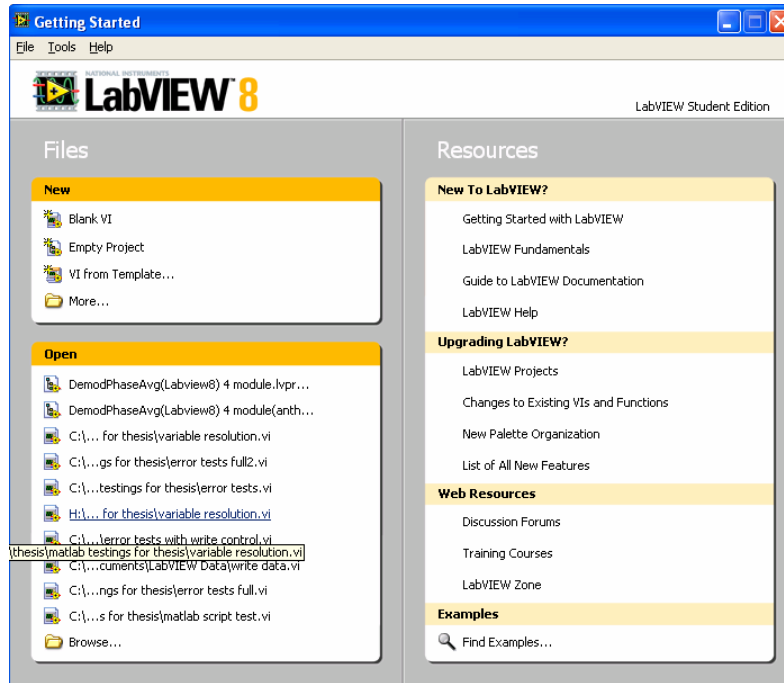


Figure 27. LabView 8.0 – Main Control Software.

One of the main challenges of using the LabView software, besides the steep learning curve, was the ‘instability’ of the embedded MATLAB scripts. There were numerous occasions where the LabView program would show error messages relating to the MATLAB script. Small changes to the script such as changing the value of a variable are at times enough to halt the entire host program. Version 8.2 of the LabView will be procured by the school in December 2006 and should solve these instability issues in the initial version 8.0 release.

9. Power Supply Unit

The power supply unit, model CP323-A Dual Output, shown in Figure 28, was purchased from CONDOR DC power supplies and provides two linear controlled outputs of 5 volts and 12 volts. The power supply unit was manufactured for OEM use and did not include any wiring harnesses or cables for powering the unit itself. Wiring for power distribution had to be added for our application. In order to provide the demodulator boards with a VGIN of 0.38V, Bob Broadston designed and built a variable voltage supply by using the 12V source from the power supply unit.



Figure 28. Dual-Output Power Supply Unit.

C. IMPLEMENTING AND TESTING RSNS ALGORITHM IN LABVIEW

The MATLAB simulations provided a basis for starting the software development for the demonstration array. As mentioned previously, all the NI modules were controlled by means of the LabView program. The block diagram in Figure 29 shows the signal processing for the determination of estimated AOA.

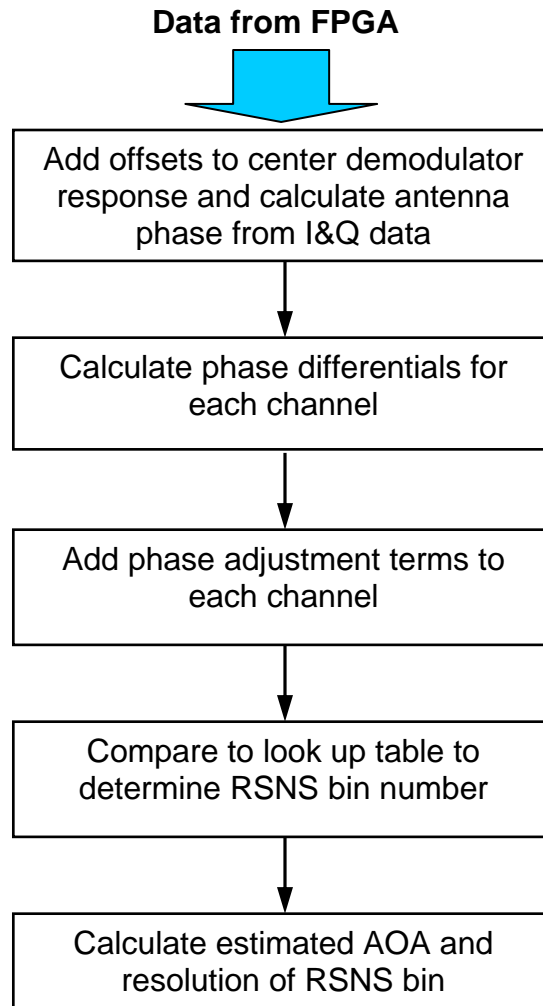


Figure 29. Block Diagram for RSNS Signal Processing.

The program consists of two major segments. The first segment deals with initializing and calibrating the modules and subsequently sampling and digitizing the I/Q differential voltage outputs from the demodulator boards. The second segment deals with the signal processing. The I/Q and rotational offsets are added to the raw I/Q signal and a moving average of 50 data points was used to calculate the signal phase. These phase data are fed into an embedded MATLAB script for the RSNS-algorithm implementation.

At the early stages, the LabView program development was conducted in its two separate segments, in two separate virtual instrument (VI). For the first segment, the Human Machine Interface (HMI), shown in Figure 30, was designed to display and plot key information such as the instantaneous and averaged I/Q data.

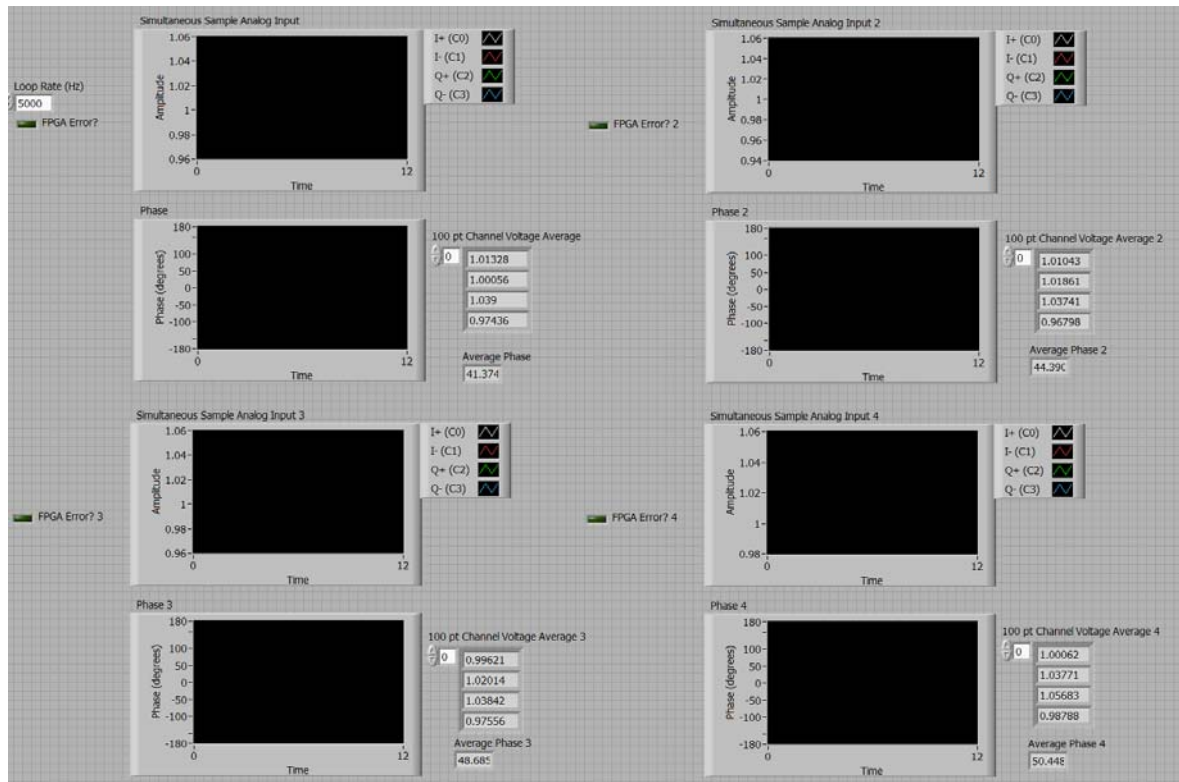


Figure 30. HMI for Initial Development (LabView Front Panel).

The second segment shown in Figure 31, where the main interest was to embed the RSNS-algorithm as a MATLAB script, was initially developed as a 'LabView Simulator' for testing of the RSNS-algorithm at a time when the hardware was not ready. The signal AOA, phase errors and antenna element distance errors were programmed as user inputs. The embedded MATLAB script shown in Figure 32 and 33 calculates the phase differentials, expected normalized voltages followed by the estimated AOA. This allowed testing the

robustness of the algorithm and provides a comparison of the theoretical phase differentials versus that obtained on the demonstration array.

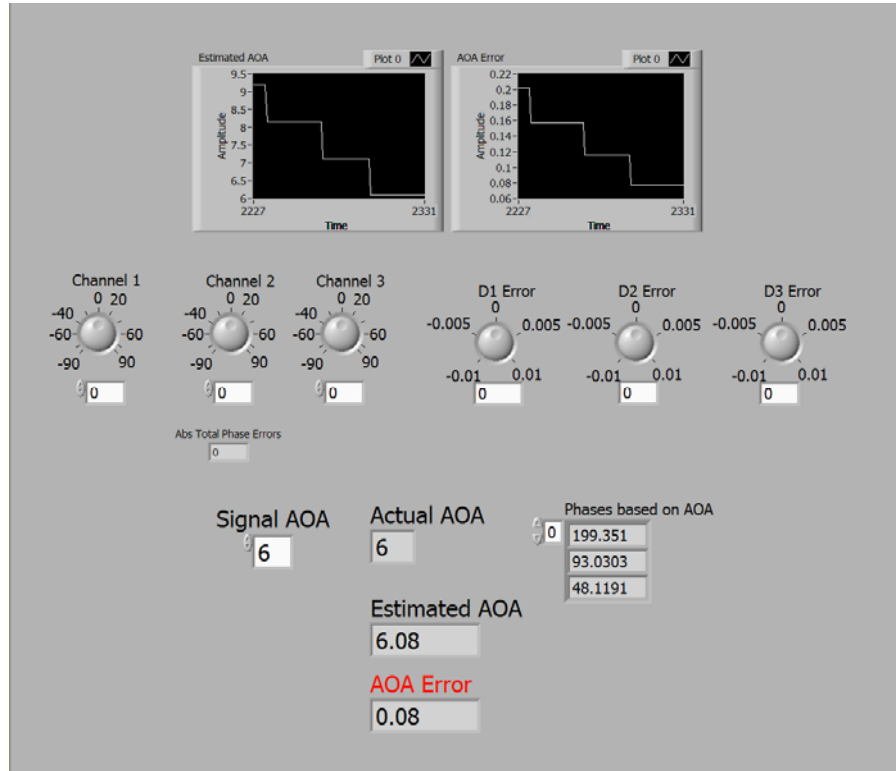


Figure 31. LabView Simulator for RSNS-Algorithm (Front Panel).

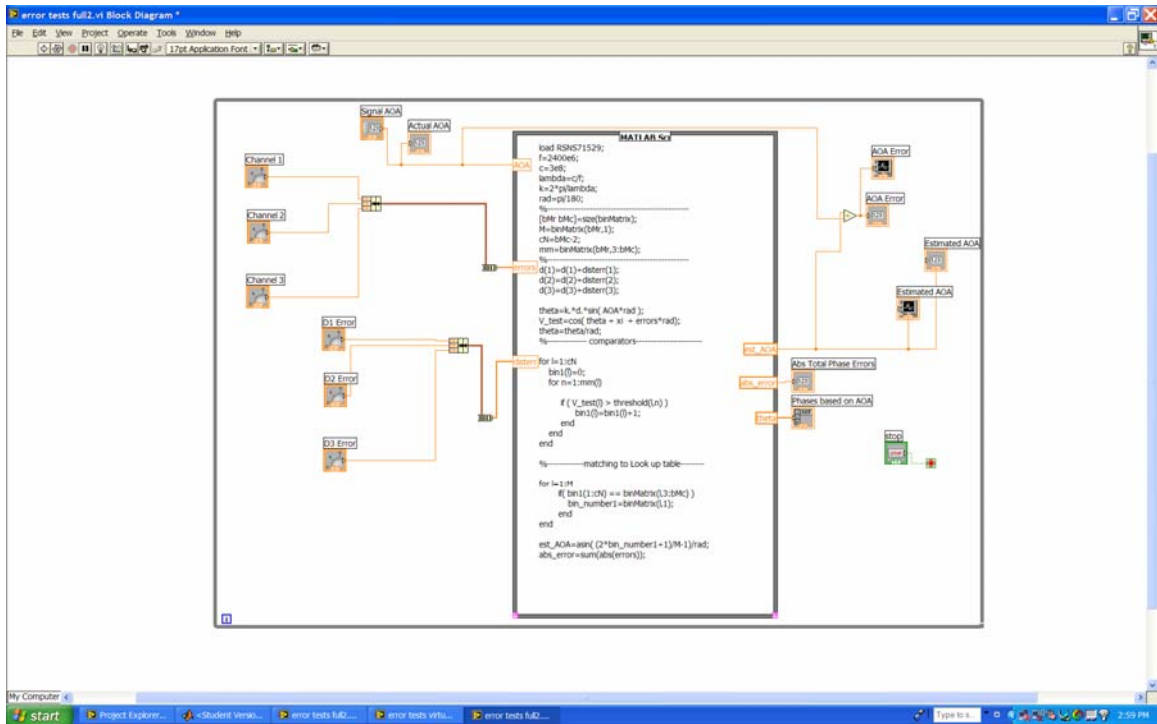


Figure 32. LabView Block Diagram for LabView Simulator.

On satisfactory testing on both LabView VI for the hardware and RSNS-Algorithm, the programs were combined, with the phase information fed as inputs into the MATLAB script.

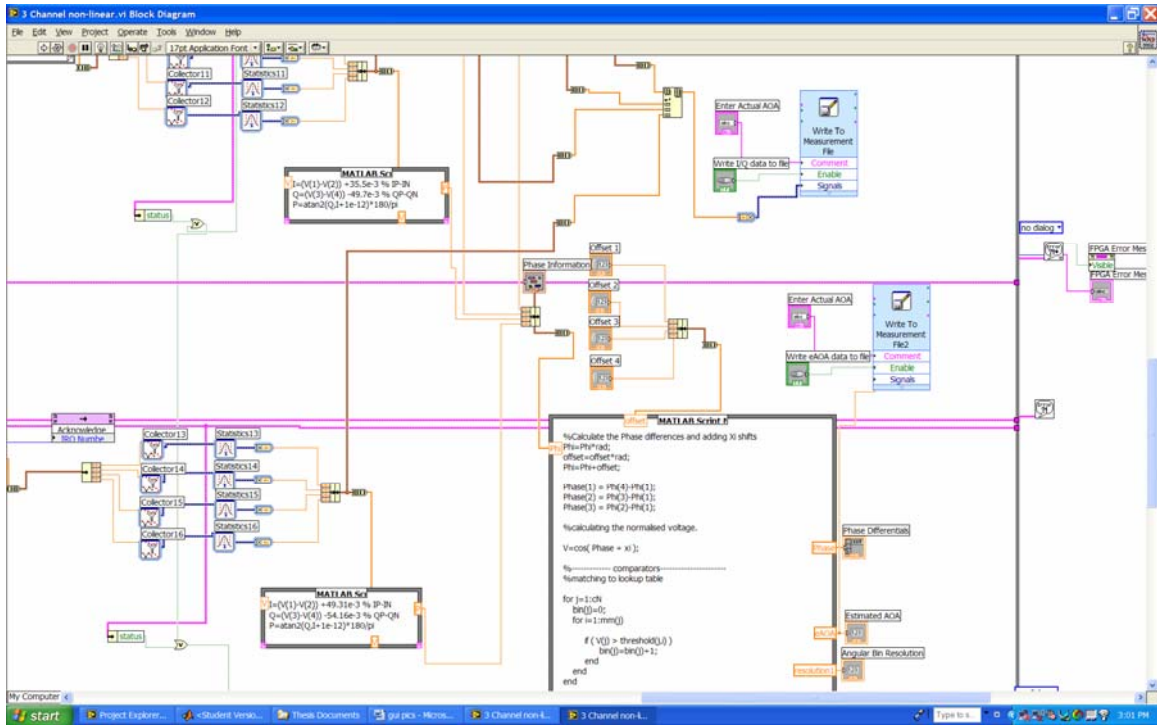


Figure 33. LabView Block Diagram after Combining both Vis.

D. SUMMARY

In this chapter, we have described both the hardware and software aspects of implementing the RSNS-based DF demonstration system. In the next chapter, we shall cover the results and analysis of the tests conducted on the demonstration system.

THIS PAGE INTENTIONALLY LEFT BLANK

VI. RESULTS AND ANALYSIS – ANTENNA ARRAY USING MODULI {7 15 29}

The assembly of the hardware components and initial testing of the RSNS algorithm, which was embedded as a MATLAB script in LabView, was completed in September 2006. In this chapter, the observations, results and analysis are listed in chronological order.

A. CALIBRATION AND PREPARATION TESTS

The demodulator calibration offsets, listed in Table 11, were used to center the demodulator I/Q response to provide a linear phase response. Each demodulator board was tested after calibration. The key observations and results of the tests conducted in the Microwave Lab are:

1. Centering I/Q Response of Demodulator Boards

The phase errors of the demodulator boards were measured by subtracting the demodulator response versus the input signal phase from the VNA. Errors up to 9 degrees were still observed on the individual boards even after several rounds of calibration and fine-tuning. Errors up to 15 degrees were observed when the phase differential was measured by taking the phase difference between the reference antenna element to the respective channel antenna. The I/Q offsets worked well for various input RF powers but needed to be re-calibrated if the VGIN (and therefore gain) on the demodulator board was varied. Same here

2. Rotation of Phase Response in Demodulator Boards

A broadside signal was simulated by feeding the output from the VNA through a 4-way power splitter to each LNA. In order to calibrate the demonstration array for a correct estimated AOA for a signal from broadside, a second rotational offset is required. The rotational offsets were used to provide a

zero phase reading for signal arriving at broadside. With all antenna phases corrected to zero, all 3-channel phase differentials were likewise zero. It was observed that the rotational offsets changed from day to day, and at times even intraday, albeit at smaller amounts. Each time the demonstration array was tested, a short calibration to update the rotational offsets was required.

3. Noise of Demodulator Boards

The overall noise in the demonstration array results in large swings in the instantaneous I/Q differential voltage outputs of the demodulator. In order to reduce these large errors, a moving average was added in the signal processing to smooth out the I/Q data. An initial moving average of 1000 points was used for the calibration process to determine the I/Q offsets. The calibration program only runs one ADC at a time, allowing it to run relatively swiftly and collect the required 1000 data points. As the LabView program was expanded to accommodate 4 elements, the program speed dropped significantly. The moving average was subsequently dropped to a 50 data point average as it improved the program speed without significant adverse impacts on the smoothing capability. With a 50 point moving average, phase differential errors up to 20 degrees were observed, with errors usually capped to within 10 degrees. It should be noted that the noise error is cumulative with the I/Q center errors. By varying the signal phase through phase shifters, total phase differential errors of up to 30 degrees were observed at times.

4. Power of Local Oscillator Input to Demodulator Board

The specifications for the demodulator board recommend a LO input power of 0 dBm to -10 dBm. It was noted that the phase response of the demodulator boards shifted when the LO power was varied. All calibrations for the boards were conducted at -8 dBm and this power was maintained at a similar level when testing was conducted in the anechoic chamber.

B. INITIAL TESTS AT ANECHOIC CHAMBER

Testing at the anechoic chamber began in early October 2006. During the initial tests, the demonstration array did not work and provided erroneous estimated AOA. The LabView simulation program was used to compare the theoretical phase differentials versus those obtained from the demonstration array. The numbers did not match. The array was eventually brought back into the lab for trouble-shooting. The key observations and analysis on the initial test are:

1. Alignment of the Array

It was not possible to physically align the reference antenna to the transmit horn antenna in a direct line of sight. The DF antenna had to rest balanced on the pedestal and was lower than the transmit antenna by approximately four inches. Given the weight of the DF system and the size of the pedestal, the center of transmit antenna was aligned to the center of the DF antenna array rather than the reference antenna.

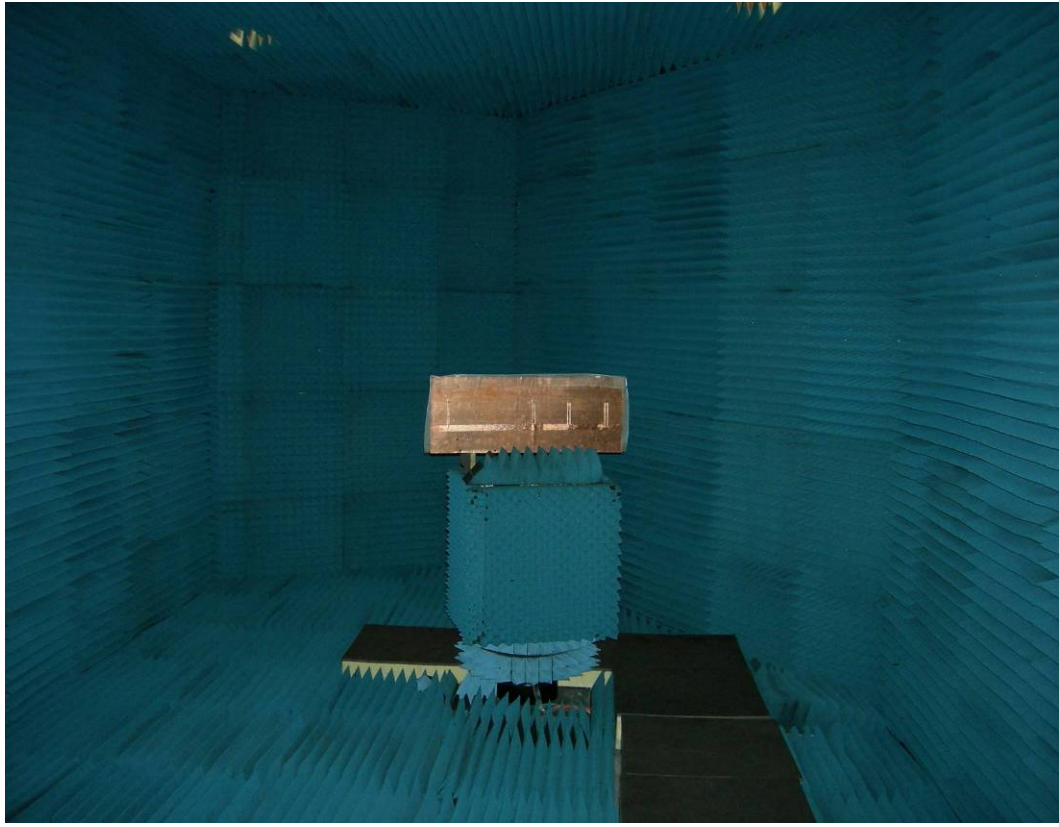


Figure 34. Testing of Demonstration Array in Anechoic Chamber.

2. Construction of Anechoic Chamber and RF Reflections

The chamber was designed mainly for peak absorption at a frequency of 3 GHz. At our operating frequency of 2.4 GHz, part of the transmitted signal would reflect off the chamber walls. The chamber was not constructed in a full rectangular shape due to space constraints. The right wall, shown in Figure 34, was at an oblique angle. This causes reflections from this wall to fall on the array either as multi-path when the array was facing the wall, or as interference into the cards and cables when the rear of the DF system is facing the wall. It is difficult to quantify the adverse effects on the DF accuracy of the demonstration array.

3. Demodulator Rotation Calibration

The rotation calibration values had to be updated each time the system was powered up, with the calibration values changing on an intra-day basis. This is in-line with the observations during the lab tests.

4. Phase Differentials on Changing Signal AOA

The phase differentials obtained from the DF array were compared to the LabView simulator. It was observed that there were very large changes in the phase differentials as the AOA was varied. This was eventually found to be a simple coding error as the average phase data from each element was not converted to radians as required in MATLAB. However, the DF system still did not produce correct AOA estimates after this error was corrected.

5. Plane Approximation of Spherically Propagating RF Signal

In the chamber setup, we are approximating the spherically expanding RF signal from the transmit antenna as a plane wave. This gives rise to significant phase errors if the antenna array is operating in the near-field. Due to the relative size of the antenna array to the separation distance between the transmit and receive antennas, the DF system is almost in the near-field.

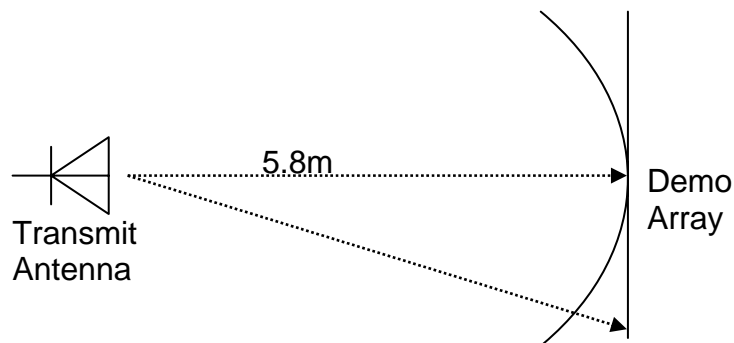


Figure 35. Plan View Showing Plane Wave Approximation.

Based on the operating frequency of 2.4 GHz and the physical dimensions where the center of the transmit antenna is aligned with the center of the demonstration array, the phase difference at the antenna at the ends of the array was -15 degrees as compared to the phase at the center of the array.

This error due to the plane wave approximation was largely calibrated out. When the rotational offsets of the demodulator response are determined in the chamber, the phase error due to the plane wave approximation is completely eliminated. However, this is only true at broadside, where the rotational offsets are determined. As the pedestal is rotated to change the signal AOA, a small error still exists.

C. TROUBLESHOOTING AT MICROWAVE LAB

After several attempts to no avail to successfully operate the demonstration array at the chamber, the DF system was brought back into the microwave lab for testing. The following faults were found:

1. Demodulator Operating Mode

A through check on the system revealed that all demodulator boards, less the board used for the reference antenna, had jumper LK3 closed instead of open. These boards were wired for AGC mode instead of VGIN mode. This error was quickly corrected.

2. Defective Components

All the system components were tested again for defects. The dipole antenna for the reference antenna was found to be faulty due to a crack in the soldering which may have occurred as we moved the DF system to the lab. Another dipole antenna was salvaged to replace the defective antenna element.

Another round of calibration was also conducted with the RF and the LO input powers to the demodulator boards tweaked to -30 dBm and -8 dBm

respectively to match the exact testing conditions in chamber. This yielded I/Q calibrations that matched the previous tests.

D. SECOND ROUND OF ANECHOIC CHAMBER TESTS

With the detected errors on the DF system corrected, the DF array was brought up to the chamber for the second round of tests. Anxious enthusiasm rapidly receded and became disappointment as the DF system continued to produce erroneous estimated AOA results, even at small AOA. With the hardware thoroughly tested, trouble-shooting efforts turned to the software and the RSNS-algorithm. The fault was finally found to reside in the how the phase differentials were determined. In the RSNS algorithm, the first modulus corresponds to d_1 , the distance of the longest baseline. In the implementation, the phase differentials were assigned in the opposite manner, with the phase differentials for the longest and shortest baselines inter-changed. Once this error was corrected, reasonably good AOA estimates were obtained. The first set of results was collected at 5 to 15 degree intervals over ± 65 degrees AOA. The results are tabulated in Table 13 and plotted in Figures 36 and 37.

Actual AOA	Estimated AOA	Error	Error Squared
-65	-70.68	-5.68	32.2624
-55	-59.61	-4.61	21.2521
-45	-47.81	-2.81	7.8961
-30	-31.95	-1.95	3.8025
-15	-15.81	-0.81	0.6561
-5	-5.298	-0.298	0.088804
0	0.129	0.129	0.016641
5	6.07	1.07	1.1449
10	10.774	0.774	0.599076
15	15.546	0.546	0.298116
25	26.339	1.339	1.792921
30	30.149	0.149	0.022201
45	44.825	-0.175	0.030625
55	53.087	-1.913	3.659569
65	61.718	-3.282	10.77152

Table 13. Initial Results from Demonstration Array.

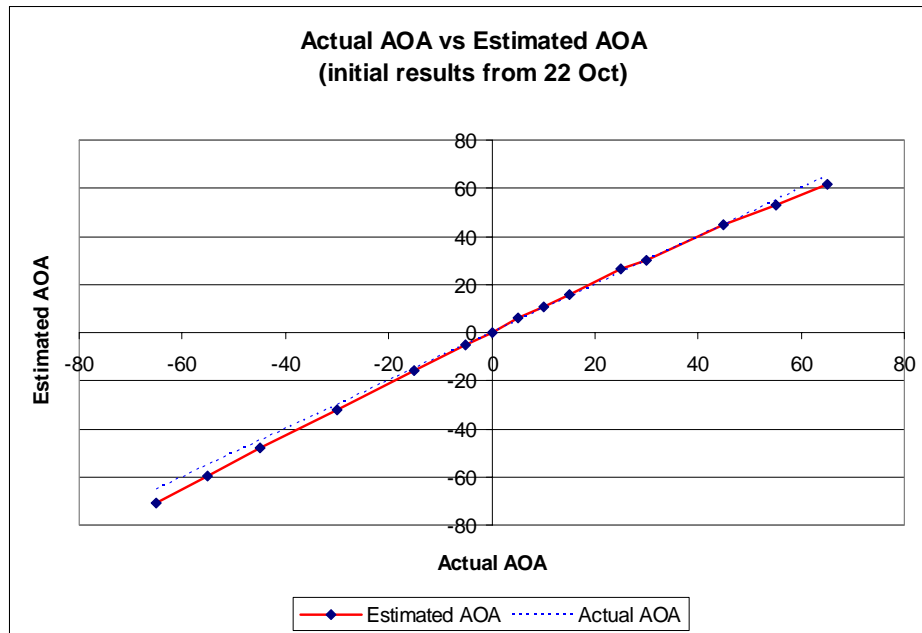


Figure 36. Initial Results from Demonstration Array.

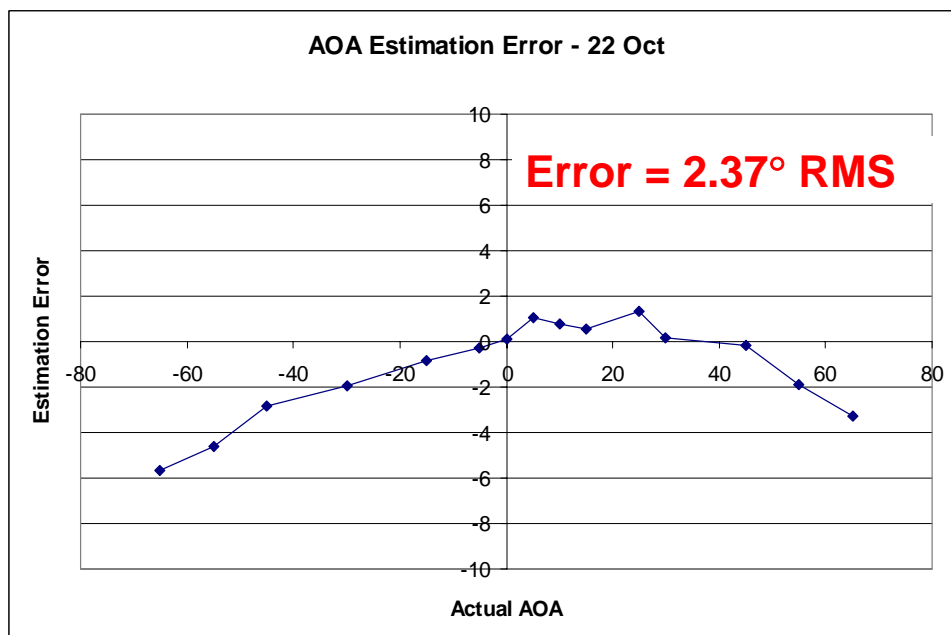


Figure 37. Initial Results – AOA Estimation Error.

The initial results were taken without ensuring that the DF antenna array was squared in parallel with the transmit horn antenna. Data points taken were also in large increments. Examining Figure 37, it can be seen that the AOA estimation error increases as the AOA is increased. Gross errors, which are very large erroneous AOA estimates, were not observed. The overall DF accuracy, defined in root mean square (RMS), was **2.37 degrees RMS**.

E. THIRD ROUND OF ANECHOIC CHAMBER TESTS

Efforts were taken to improve the accuracy of the DF system. Several steps were taken, including:

1. Raising the DF Array Platform

The entire array was raised by 4 inches as shown in Figure 38. This was done to line up the height of the DF array to transmit horn antenna. It also eased the connection of the LO signal, Ethernet cable and power cables from the DF system into the pedestal cavity.

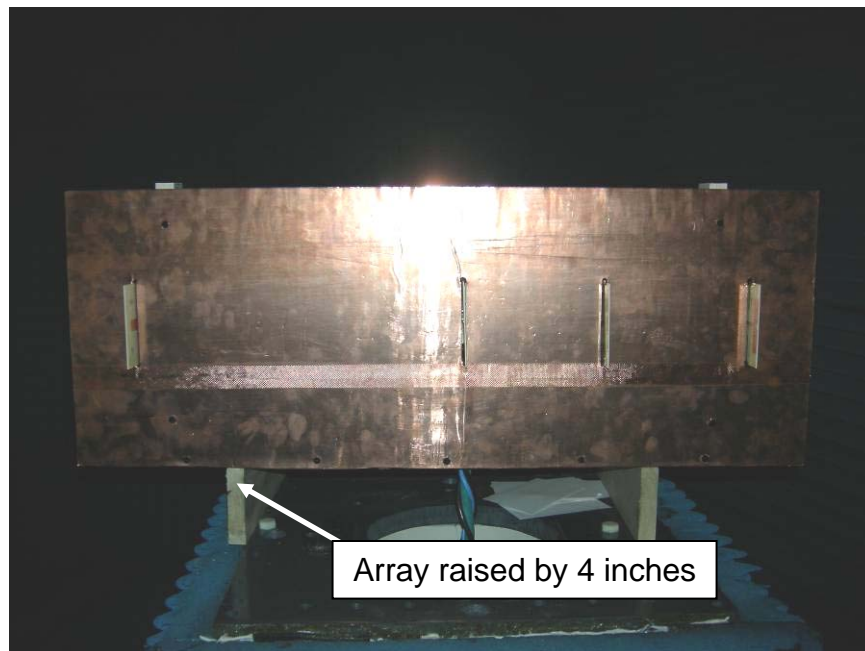


Figure 38. Front View of DF System on Pedestal.

2. Grounding Unused Demodulator Terminals

Small voltages were detected at the unused terminals of the demodulator boards, varying from 5 to 15 mV. These unused terminals were connected to ground as shown in Figure 39.

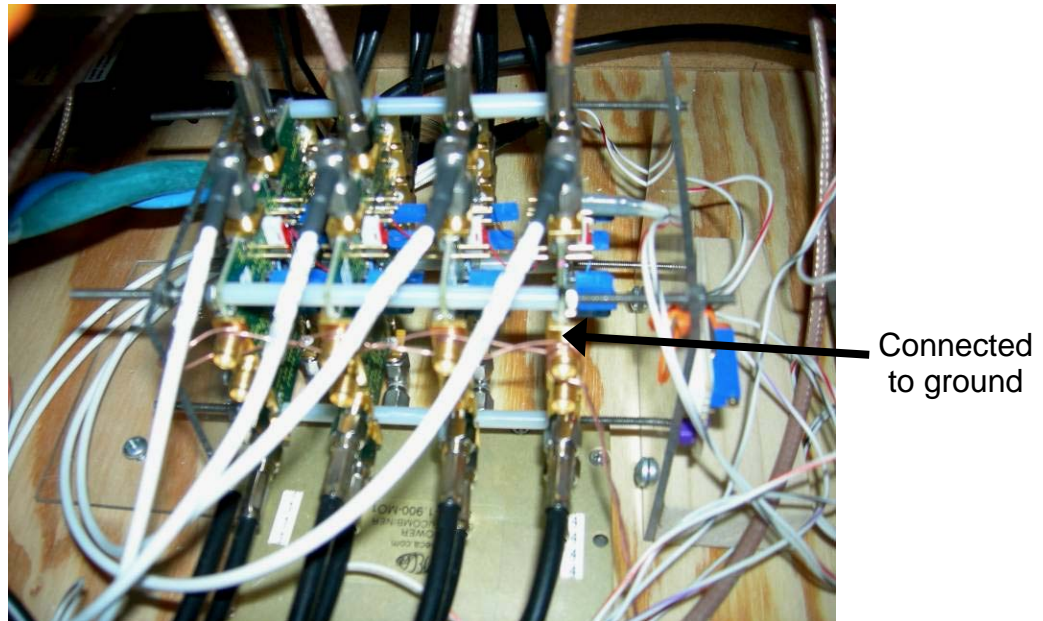


Figure 39. Grounding Unused Demodulator Terminals.

3. Shielding for DF Array

In order to minimize the effects of the transmitted RF signal from reflecting off the walls and adversely affecting the system, a crude shielding was made from metal netting and draped over the entire DF system and connected to ground as shown in Figure 40.

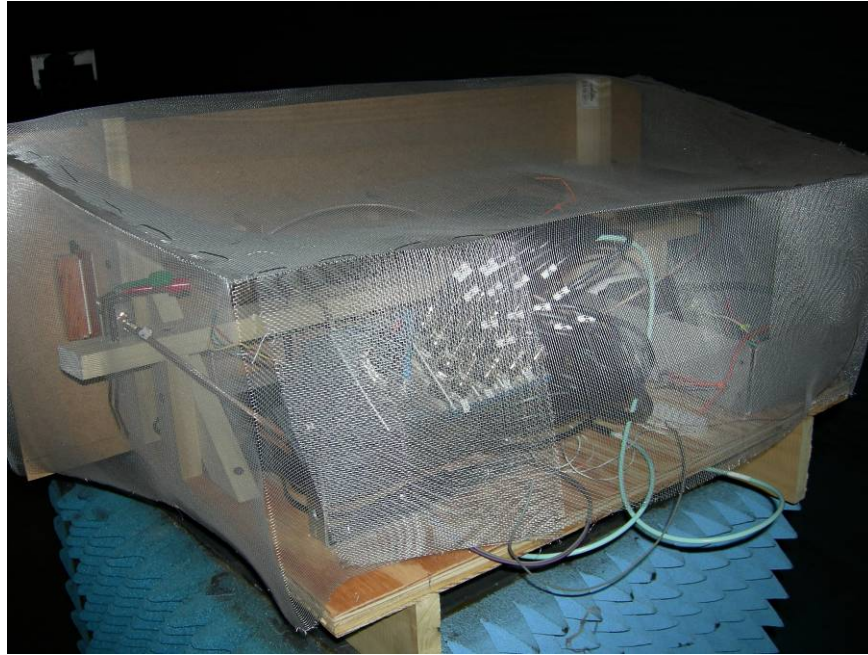


Figure 40. Shielding for DF System.

4. Aligning DF Array with Transmit Antenna

In order to align the DF array to the transmitting horn antenna, the diagonal distances were measured as shown in Figure 41 and the DF array adjusted to equalize the distances. This provides an alignment accuracy of approximately one degree.

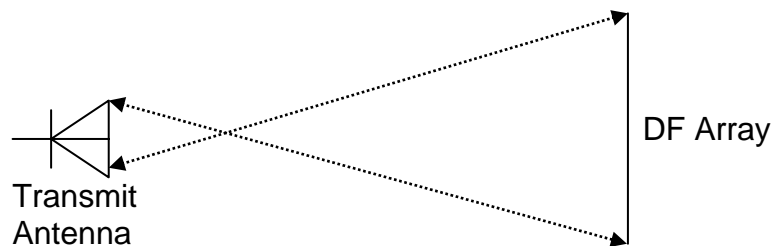


Figure 41. Aligning DF Array to Transmit Antenna.

With the modifications complete, the DF array performance was tested again and data was taken at 5 degree intervals over ± 60 degrees as shown in Table 14 and plotted in Figure 42.

AOA	eAOA	Error	Error Squared
-60	-61.1785	1.178534	1.388942
-55	-56.6769	1.676863	2.81187
-50	-51.401	1.401016	1.962846
-45	-46.6753	1.675337	2.806754
-40	-40.9504	0.950397	0.903254
-35	-36.3234	1.323405	1.751401
-30	-31.0487	1.048654	1.099675
-25	-25.7652	0.765232	0.58558
-20	-19.8824	-0.11764	0.013838
-15	-15.0113	0.011268	0.000127
-10	-10.2491	0.249091	0.062046
-5	-5.03923	0.039232	0.001539
0	0.1209	-0.1209	0.014617
5	5.039232	-0.03923	0.001539
10	10.77408	-0.77408	0.599201
15	15.54636	-0.54636	0.29851
20	19.88236	0.117637	0.013838
25	25.76523	-0.76523	0.58558
30	30.74788	-0.74788	0.559322
35	35.68534	-0.68534	0.469684
40	36.32341	3.676595	13.51735
45	43.74432	1.25568	1.576732
50	49.37691	0.623088	0.388239
55	52.65951	2.34049	5.477893
60	58.60581	1.394192	1.943771

Table 14: DF Performance – 2nd Set of Results

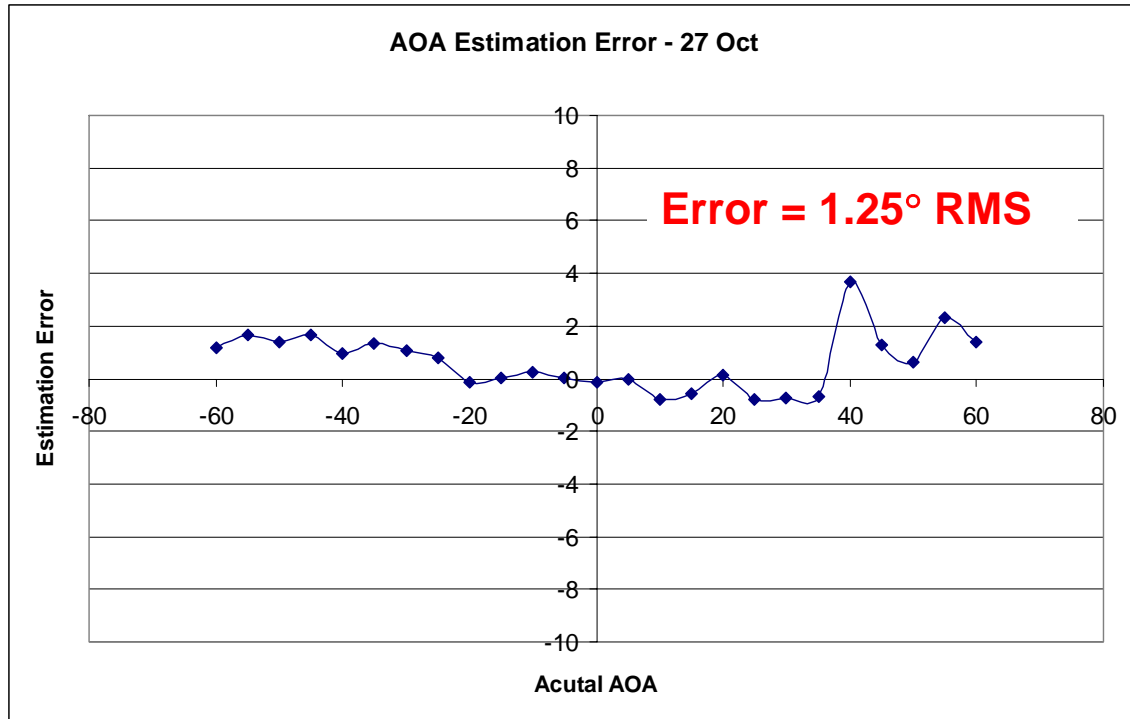


Figure 42. AOA Estimation Error – 2nd Set of Results.

The plot of AOA estimation error (Figure 42) shows that the errors at large AOA have been significantly reduced and shows that steps taken to minimize errors were successful. The overall error has been reduced to **1.25 degrees RMS** and compares favorably against the initial results of 2.37 degrees RMS. The characteristics of the error from both tests are similar; AOA estimation error increases correspondingly with signal AOA.

The main error sources likely come from a combined contribution from antenna spacing errors and phase errors from the demodulator boards. Since these errors were minimized as much possible in during the design and building stages, we have optimized the DF array performance within our means, given the constraints of the materials and hardware available.

F. UPDATING HMI AND IN-DEPTH DF PERFORMANCE

Although gross errors were not captured in results of the 2nd data set, several gross errors were observed as the signal AOA was scanned across the FOV. These gross errors occurred in the region around ± 20 and ± 40 degrees. It was necessary to take a set of results with a higher resolution to provide a clearer picture on the performance of the DF system.

1. Updating Human Machine Interface

The intention was to capture a data set with AOA increments of 0.5 to 1 degree intervals over the FOV. This would be very time consuming as the pedestal control program and the LabView program for the DF system were housed on two separate computers and was not linked. All data sets were previously recorded by hand.

It was timely to update the HMI, which up to this point, was largely designed for troubleshooting and displaying system data. The HMI was re-organized for a friendlier user interface to show only key information.

Two 'write-to-data-file' buttons were also added. The first button captures all 16 raw differential outputs without the center or rotational offsets. This provides real data to be captured for post-analysis to determine the exact phase differential errors present in the DF system. The data would also be used to optimize the I/Q center offsets or testing the performance of virtual moduli sets.

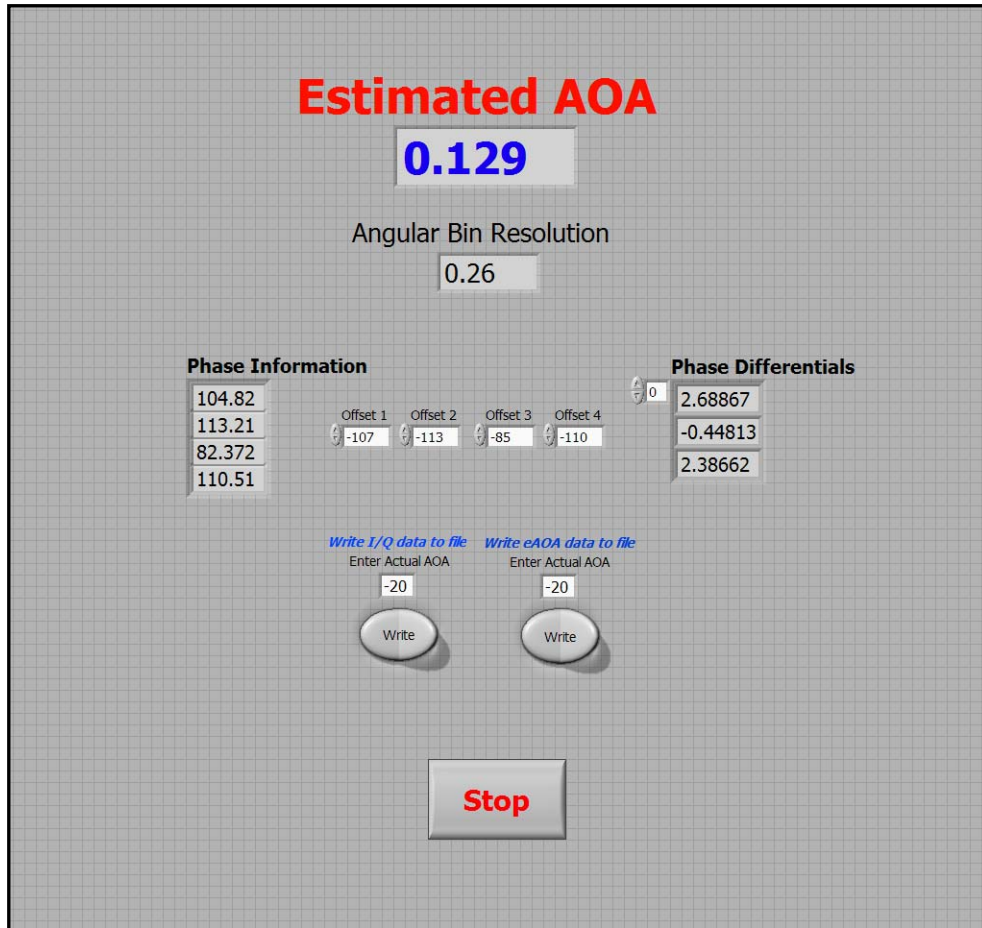


Figure 43. Updated HMI with Write-to-File Capability.

The new HMI as shown in Figure 43 provides a very 'clean' operating environment and clearly displays the estimated AOA and the respective angular bin resolution size. Phase information is still kept on the HMI as this is required for the calibration of the rotation offsets.

2. Detailed DF Performance

With the HMI updated, a detailed data set of the DF performance was captured and the AOA data saved to a LabView data file. The data file was exported to excel for plotting.

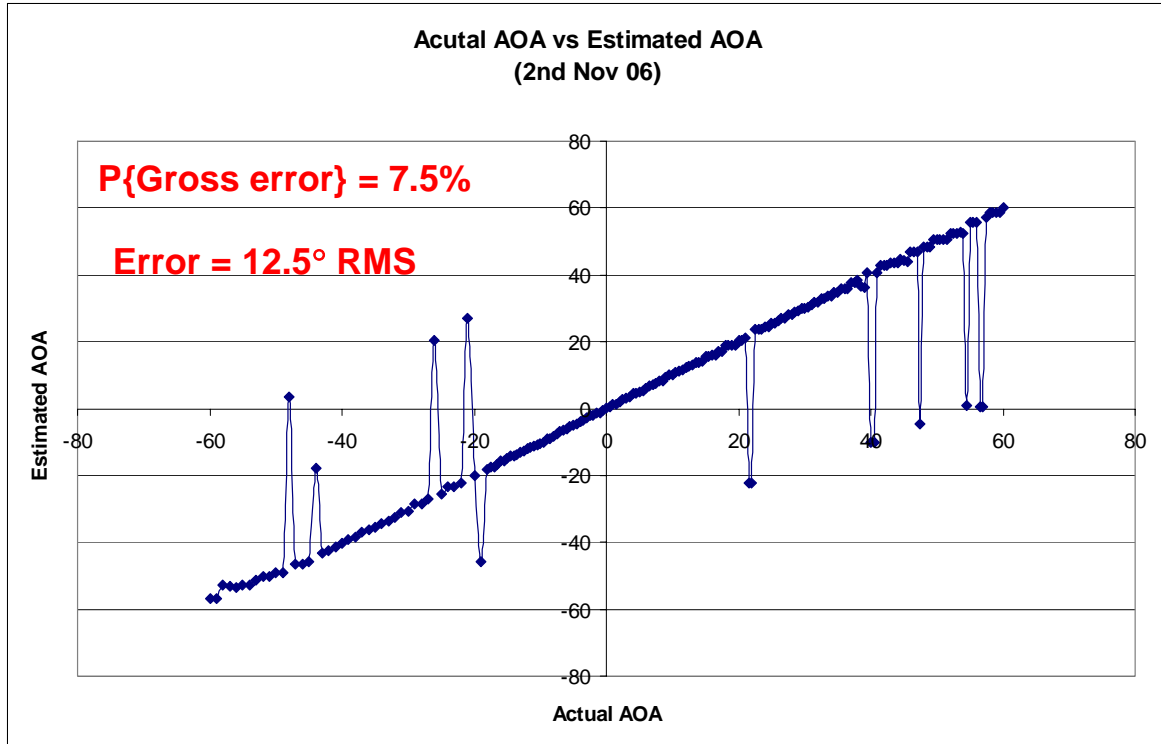


Figure 44. DF Performance – 3rd Set of Results.

Examining the results as shown in Figure 44, it is evident that gross errors occur at a number of AOAs. In total, there were 16 gross errors out of 208 data points, resulting in a probability of gross error of 7.5%. Taking these gross errors into consideration, the overall DF accuracy has dropped significantly to 12.5 degrees RMS. If the gross errors were eliminated, the DF accuracy is a remarkable 0.7 degree RMS with a baseline of 66 cm.

G. SUMMARY

The hardware and software for the demonstration system was successfully implemented. Excellent results were achieved with the digital architecture which provided flexibility signal processing. Some gross errors were observed, likely resulting from noise in the demodulator boards and antenna spacing errors. In the next chapter, we will examine the virtual spacing concept and present the results of a second array built for evaluating the concept.

VII. RSNS INTERFEROMETRY WITH VIRTUAL SPACING

In this chapter, we will first review the method of designing a two-channel virtual spacing RSNS interferometer as introduced by [7] and then extend the concept for N -channel systems.

At the onset, the virtual spacing concept was found to be only applicable for a two-channel system. In working with our original antenna array which used a PRP moduli set of $\{7\ 15\ 29\}$, many months were spent attempting to extend the virtual spacing concept to accommodate a three-channel system, to no avail. Nonetheless, the plan was to proceed in building the demonstration DF system. The virtual spacing concept for the three-channel system would then be used on the same antenna array when a suitable algorithm for the three channel system was found.

The breakthrough came about in late October, where a closed form solution applicable for N -channel systems was found for non-PRP moduli sets. The original hardware and control software used for the first array were modified to accommodate a new 3-channel antenna array which had to be built as a different set of non-PRP moduli was used. The modifications and performance of the virtual spacing DF system are presented in sections C and D.

A. TWO CHANNEL RSNS INTERFEROMETRY WITH VIRTUAL SPACING

For interferometry, a channel is composed by taking measurements of the phase differential between the reference antenna r and antenna element n . The in-phase and quadrature output for a channel can be defined as

$$\begin{aligned} V_{in}(\theta) &= \cos(kd_n \sin \theta) = \cos(\Delta\phi_{rn}) \\ &= \cos(\phi(p_n))\cos(\phi(p_r)) + \sin(\phi(p_n))\sin(\phi(p_r)) \\ &= V_{in}V_{ir} + V_{Qn}V_{Qr} \end{aligned} \tag{7.1}$$

$$\begin{aligned}
V_{Qn}(\theta) &= \sin(kd_n \sin \theta) = \sin(\Delta \phi_m) \\
&= \sin(\phi(p_n)) \cos(\phi(p_r)) - \cos(\phi(p_n)) \sin(\phi(p_r)) \\
&= V_{In}V_{Ir} - V_{Qn}V_{Qr}
\end{aligned} \tag{7.2}$$

where d_n is the distance between element n and the reference element r .

Consider a two-channel RSNS interferometer with the moduli pair m_1 and m_2 with the dynamic range \hat{M} . The I and Q terms for the two channels can be combined in the following manner

$$V'_{I1} = \cos(k(d_1 + d_2) \sin \theta) = \cos(kd'_1 \sin \theta) \tag{7.3}$$

$$V'_{Q1} = \sin(k(d_1 + d_2) \sin \theta) = \sin(kd'_1 \sin \theta) \tag{7.4}$$

$$V'_{I2} = \cos(k(d_1 - d_2) \sin \theta) = \cos(kd'_2 \sin \theta) \tag{7.5}$$

$$V'_{Q2} = \sin(k(d_1 - d_2) \sin \theta) = \sin(kd'_2 \sin \theta) \tag{7.6}$$

These new voltages can now be regarded as the in-phase and quadrature components of a new 2-channel interferometer with virtual spacing of d'_1 and d'_2 . In designing the distances between elements, the following relationship is used

$$d_i = n_i \frac{\lambda}{2} = \frac{\hat{M}\lambda}{4Nm_i} \tag{7.7}$$

For a fixed operating frequency and using the same moduli set, the wavelength and dynamic range are constants. Moduli sets are usually defined from the smallest modulus number sequentially to the largest modulus numbers. Since the modulus is a denominator in Equation (7.7), it should be noted that the distance d_1 is, therefore, the longest distance in the antenna array. The new virtual spacing of ($d'_2 = d_1 - d_2$) is, therefore, a positive value. Choosing the relationship between the moduli as

$$m_2 = hm_1 \tag{7.8}$$

results in the ratio h larger than unity as $m_2 > m_1$. Expanding the new virtual spacing using Equation (7.7) results in

$$d'_1 = d_1 + d_2 = \frac{\lambda \hat{M}}{4N} \left(\frac{1}{m_1} + \frac{1}{m_2} \right) \xi = \frac{\lambda \hat{M}}{4N} \left(\frac{h+1}{m_2} \right) \xi = \frac{\lambda \hat{M}}{4N m'_1} \xi' \quad (7.9)$$

$$d'_2 = d_1 - d_2 = \frac{\lambda \hat{M}}{4N} \left(\frac{1}{m_1} - \frac{1}{m_2} \right) \xi = \frac{\lambda \hat{M}}{4N} \left(\frac{h-1}{m_2} \right) \xi = \frac{\lambda \hat{M}}{4N m'_2} \xi' \quad (7.10)$$

Simplifying the equations results in

$$d'_1 = \hat{M} \xi' \left(\frac{h+1}{m_2} \right) = \frac{\hat{M}}{m'_1} \xi' \quad \text{and} \quad d'_2 = \hat{M} \xi' \left(\frac{h-1}{m_2} \right) = \frac{\hat{M}}{m'_2} \xi' \quad (7.11)$$

Dividing these two equations yields

$$\left(\frac{h+1}{h-1} \right) = \frac{m'_2}{m'_1} \longrightarrow m'_2 = m'_1 \left(\frac{h+1}{h-1} \right) \quad (7.12)$$

The virtual spacing moduli pair $\{m'_1, m'_2\}$ can now be calculated by Equation (7.12) based on h , the relationship between the original, real spacing moduli pair $\{m_1, m_2\}$. Values of m'_1 (an integer) must be selected such that m'_2 is also an integer. On determining the new dynamic range, the scaling factor for the virtual spacing interferometer can be derived from Equation (7.11) and subsequently the FOV from the new scaling factor.

It is generally possible to obtain virtual spacing moduli pairs $\{m'_1, m'_2\}$ that are both integers, as only one ratio maps their relationship. Higher multiples of the new moduli pair can also be used to achieve increasingly higher resolution, so long as its FOV is within acceptable limits and the system SNR is able to support reasonably error-free RSNS coding.

Several examples have been worked out in [7] with the consideration of original and virtual moduli which are pairwise relatively prime (PRP) or otherwise.

B. N-CHANNEL RSNS INTERFEROMETRY WITH VIRTUAL SPACING

For error-free coding, we require RSNS moduli sets to be comprised of integer-valued modulus. In designing a two channel system with virtual spacing, we need only to contend with a single ratio $(h+1)/(h-1)$ and select the first

modulus that ensures that the second modulus is also integer-valued. In an N -channel system, we need to contend with $(N-1)$ ratios. Depending on the relationships between the individual modulus, it may not be possible to select m_1' such that all subsequent moduli are also integer-valued.

The N -channel algorithm operates only for original moduli sets where the ratio between the first modulus and the subsequent moduli is $h^{(n-1)}m_n$. The following relationship between the moduli would be

$$m_1 = hm_2 = h^2 m_3 \dots = h^{(n-1)}m_n \quad (7.13)$$

Note that this relationship is defined differently from the two channel case, where $(m_2=hm_1)$. Following a similar treatment as in the two channel system, we obtain

$$d_1' = d_1 + d_2 = \frac{\lambda \hat{M}}{4N} \left(\frac{1}{m_1} + \frac{1}{m_2} \right) \xi = \frac{\lambda \hat{M}}{4N} \left(\frac{h+1}{m_1} \right) \xi = \frac{\lambda \hat{M}'}{4Nm_1'} \xi' \quad (7.17)$$

$$d_2' = d_1 - d_2 = \frac{\lambda \hat{M}}{4N} \left(\frac{1}{m_1} - \frac{1}{m_2} \right) \xi = \frac{\lambda \hat{M}}{4N} \left(\frac{1-h}{m_1} \right) \xi = \frac{\lambda \hat{M}'}{4Nm_2'} \xi' \quad (7.15)$$

$$\begin{aligned} d_3' = d_1 - d_2 - d_3 &= \frac{\lambda \hat{M}}{4N} \left(\frac{1}{m_1} - \frac{1}{m_2} - \frac{1}{m_3} \right) \xi \\ &= \frac{\lambda \hat{M}}{4N} \left(\frac{1-h-h^2}{m_1} \right) \xi = \frac{\lambda \hat{M}'}{4Nm_3'} \xi' \end{aligned} \quad (7.16)$$

.

.

.

$$\begin{aligned} d_n' = d_1 - d_2 - \dots - d_n &= \frac{\lambda \hat{M}}{4N} \left(\frac{1}{m_1} - \frac{1}{m_2} - \dots - \frac{1}{m_n} \right) \xi \\ &= \frac{\lambda \hat{M}}{4N} \left(\frac{1-h-\dots-h^{(n-1)}}{m_1} \right) \xi = \frac{\lambda \hat{M}'}{4Nm_n'} \xi' \end{aligned} \quad (7.17)$$

Re-arranging and simplifying the formulas gives

$$\hat{M}\left(\frac{h+1}{m_1}\right)\xi = \frac{\hat{M}_1'}{m_1'}\xi' \quad (7.18)$$

$$\hat{M}\left(\frac{1-h}{m_1}\right)\xi = \frac{\hat{M}_2'}{m_2'}\xi' \quad (7.19)$$

.

.

.

$$\hat{M}\left(\frac{1-h-h^2\ldots-h^{(n-1)}}{m_1}\right)\xi = \frac{\hat{M}_n'}{m_n'}\xi' \quad (7.20)$$

Dividing Equation (7.18) by its successive equations yields

$$\left(\frac{1+h}{1-h}\right) = \frac{m_2'}{m_1'} \quad (7.21)$$

$$\left(\frac{1+h}{1-h-h^2}\right) = \frac{m_3'}{m_1'} \quad (7.22)$$

.

.

.

$$\left(\frac{1+h}{1-h-h^2\ldots-h^{(n-1)}}\right) = \frac{m_n'}{m_1'} \quad (7.23)$$

Upon examination of Equations (7.21 to 7.23), one will find that the denominator will always be positive as h is <1 based on the relationship outlined in Equation (7.13).

C. VIRTUAL SPACING COMBINATIONS FOR N -CHANNEL SYSTEMS

In the initial setup for the N -channel system virtual spacing, we have defined in Equation (7.14) through to Equation (7.17), a specific combination of real antenna spacing for mapping into virtual spacing. Other combination sets can be explored to achieve desired design requirements.

The longest virtual baseline that can be achieved is the summation of all real antenna spacings. Correspondingly, the shortest virtual baseline is where we subtract the all other spacings from the longest baseline. Other combinations exist and they increase with the number of channels/baselines used.

In solving for the N -channel virtual spacing, we chose a linear combination for the moduli relationship. While this allows for a closed form solution for linearly spaced antenna elements, it cannot be applied to PRP moduli sets. Different moduli relationships such as

$$m_1 = hm_2 = km_3 \quad (7.24)$$

where (k/h) is an integer, may also be possible extensions to the technique laid out and provide a solution for solving PRP moduli sets.

D. DESIGN EXAMPLE FOR 3-CHANNEL RSNS INTERFEROMETRY WITH VIRTUAL SPACING

Consider the case of $m_1=4$, $m_2=8$ and $m_3=16$. Let the scaling factor ξ be unity. For this system, the dynamic range \hat{M} is 53 with a broadside resolution of 2.16 degrees. The ratio between moduli is $h=1/2$. Applying Equations (7.21, 7.22), we obtain the relationship between the new virtual spacing moduli as

$$m'_2 = 3m'_1 \quad \text{and} \quad m'_3 = 6m'_1 \quad (7.25)$$

Some possible moduli sets and their key parameters are shown in Table 15. Additional virtual spacing sets can be used so long as their moduli conform to the relationship as given in Equation (7.25).

Moduli Set	Element Distances	Dynamic Range	Broadside Resolution	Scaling Factor	FOV
{4 8 16}	$d_1 = 0.1406$ $d_2 = 0.0703$ $d_3 = 0.0352$	53	2.16°	1	± 90
{3 9 18}	$d_1' = 0.2105$ $d_2' = 0.0702$ $d_3' = 0.0351$	59	1.92°	1.01059	± 81.7
{9 27 54}	$d_1' = 0.2083$ $d_2' = 0.0694$ $d_3' = 0.0347$	167	0.64°	1.0711	± 69

Table 15. Moduli Sets for 3-Channel Virtual Array.

The transfer function of the original set and the two virtual spacing sets, in an ideal case where noise is absent, are plotted in Figures 45 to 47.

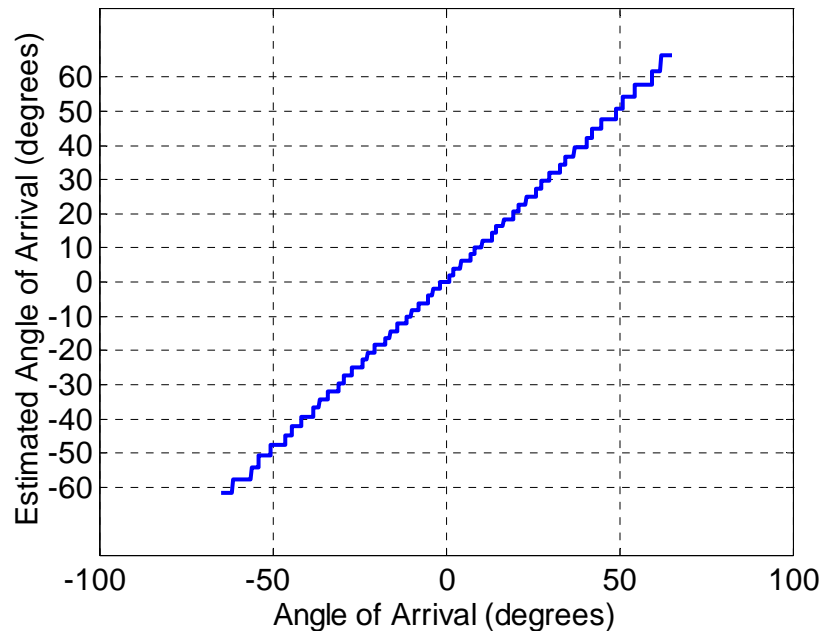


Figure 45. Transfer Function of Real Spacing using Moduli {4 8 16}.

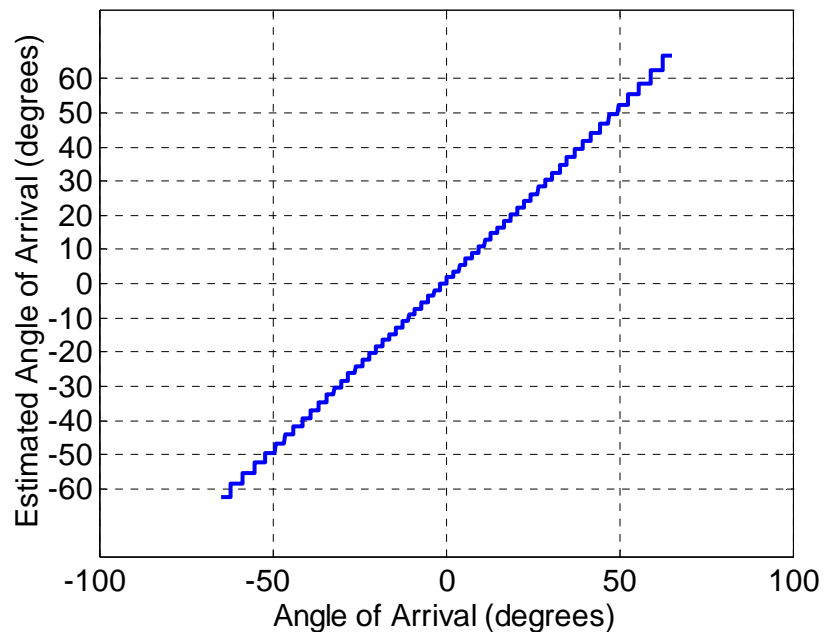


Figure 46. Transfer Function of Virtual Spacing using Moduli {3 9 18}.

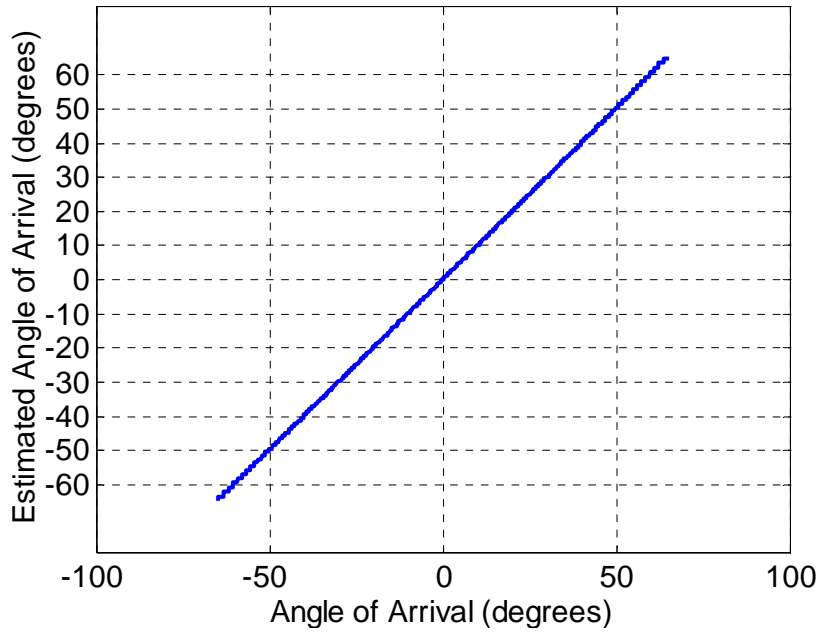


Figure 47. Transfer Function of Virtual Spacing using Moduli {9 27 54}.

In this section, the virtual spacing concept and the steps for implementing 2-channel systems and N -channel systems have been presented. For a 2-channel system, we can apply the virtual spacing concepts to both PRP and non-PRP moduli sets as we only need to deal with a single ratio and integer-valued moduli can usually be obtained. The virtual spacing concept was extended to N -channel systems with non-PRP moduli. A N -channel solution for PRP moduli has yet to be discovered.

E. BUILDING AND TESTING THE VIRTUAL SPACING DF SYSTEM

On completion of the performance tests on the first DF antenna array, a second antenna was built to test the virtual spacing concept using the design example presented in Section D. A moduli set of {4 8 16} is used for the real array and the moduli set of {9 27 54} is used for the virtual spacing concept. The key data of the RSNS parameters are presented in Table 16 and the array is shown in Figure 48.

Moduli Set	Element Distances	Dynamic Range	Broadside Resolution	Scaling Factor	FOV
{4 8 16} <i>Real</i>	$d_1 = 0.1406$ $d_2 = 0.0703$ $d_3 = 0.0352$	53	2.16°	1	± 90
{9 27 54} <i>Virtual</i>	$d_1' = 0.2083$ $d_2' = 0.0694$ $d_3' = 0.0347$	167	0.64°	1.0711	± 69

Table 16: Moduli Sets for 3-Channel Virtual Spacing Concept.



Figure 48. Antenna Array for 3-Channel Virtual Spacing Concept.

The length of the array was 14 cm, significantly shorter as compared to the first array with a length of 66 cm. Besides building a new ground plane, four

additional dipole antenna elements were tested and used for the new array. The LNAs were re-located and aligned with the new antenna locations.

The virtual spacing algorithm is a simple iterative process. The estimated AOA's are calculated in sequence, starting with the real spacing. The estimated AOA from the real spacing was the most reliable and was defaulted as the initial accepted estimated AOA. The selection criteria for reported estimated AOA was based on a user defined threshold, specified in terms of the number of resolution cells of the current accepted estimated AOA. A simplified signal processing flow diagram shown in Figure 49 explains the process.

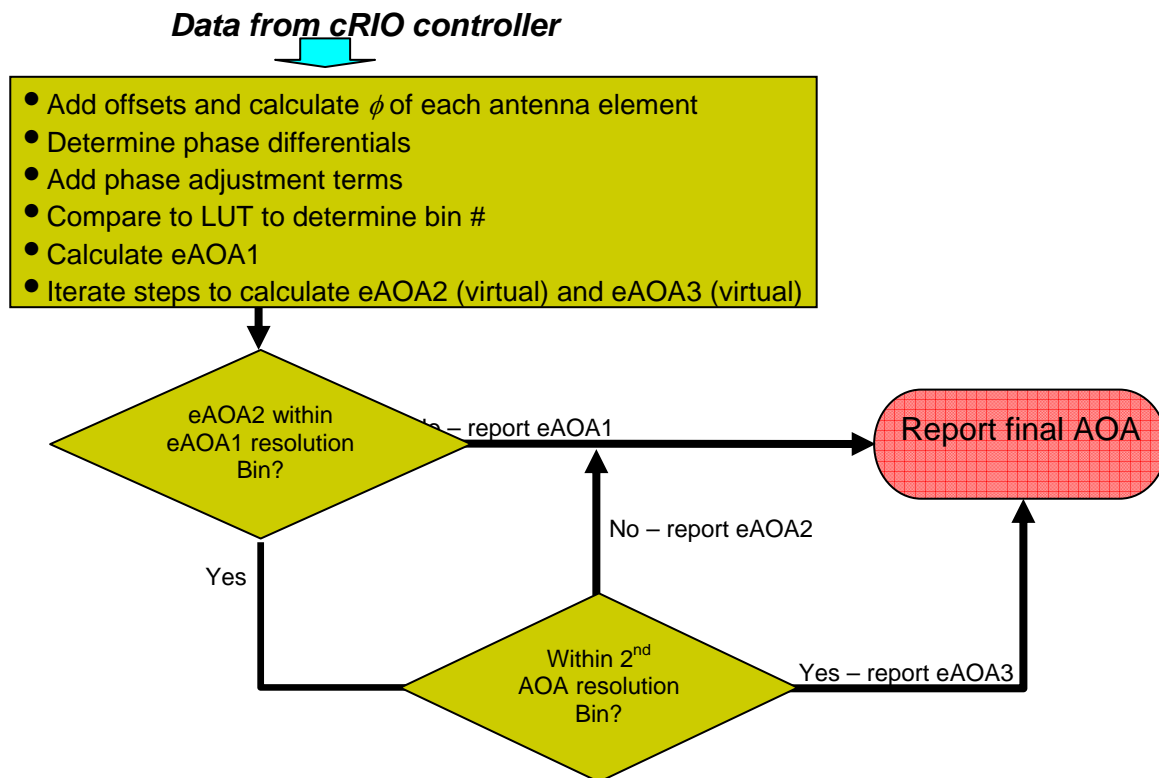


Figure 49. Simplified Flow Diagram for Virtual Spacing Signal Processing.

Detailed simulations in MATLAB with respect to DF accuracy under noisy conditions and the effects of antenna element spacing errors were not conducted due to time constraints. The LabView simulator program shown in Figure 50 was

modified for the virtual spacing processing. Simulations under a noise free-environment showed that it was possible to achieve error-free ‘super-resolution’ by simply continually increasing the moduli numbers used for the virtual spacing.

It is difficult to analyze and quantify the susceptibility of the DF performance to phase errors and antenna spacing errors using the LabView simulator. The program only provides results for a single AOA value at a time. However, it was observed that as phase errors or antenna distance errors were introduced, the virtual spacing estimated AOA produced significantly more gross error estimates.



Figure 50. LabView Simulator for Virtual Spacing.

With the algorithm tested successfully on the LabView simulator, modifications were made to the LabView control program used for the first array. The new array was built with the reference antenna in the center of the ground plane, which allowed for the reference antenna to be aligned directly in-line with the transmit antenna. A data set was taken at 1 degree intervals over ± 60

degrees AOA. The experimental results were saved to a LabView data file, imported into Excel and plotted in Figure 51.

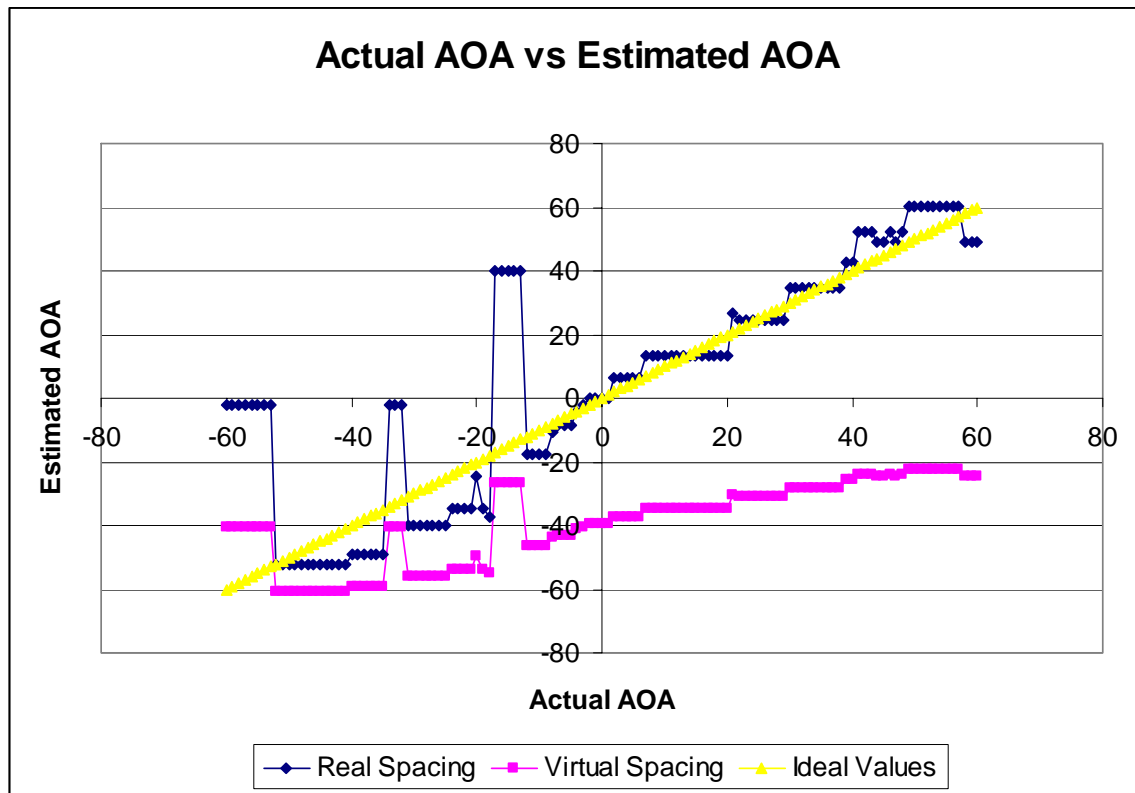


Figure 51. DF Experimental Performance for Virtual Spacing Array

Although exactly the same hardware was used, the DF performance for the real spacing (in blue) is significantly worse compared to the first array. Overall DF accuracy for the real spacing is 389 degrees RMS due to the large number of estimates with gross errors.

Results from the virtual spacing (in magenta) follow the same shape as the real spacing but appear to have a gain factor error. While it was not captured in this data set, there were several occasions where a higher resolution result, with lower AOA estimation error, was successfully provided by virtual spacing. However, this occurred only near broadside and was not observed when the AOA was increased beyond 5 degrees.

F. ERROR SOURCES FOR THE VIRTUAL ARRAY

The second array, setup for the virtual spacing, suffers from exactly the same set of errors as the first array. However, the sensitivity of the system to these errors differs.

1. Plane Wave Approximation

The size of virtual spacing array is only 14 cm, compared to 66 cm for the first array. Given the size of the virtual array and the distance between the transmit antenna and the DF array, these errors are minimal, as array is in the 'far-field'.

2. Demodulator Phase Errors

We can consider the combined demodulator errors as 'fixed constants' in terms of its maximum absolute error. For example, the maximum observed error of the demodulator boards is in the region of 30 degrees, regardless of the length of the array and the antenna spacing used.

3. Antenna Spacing Errors

Antenna spacing errors are also a relatively fixed quantity. The amount of human accuracy as we build the ground plane, measure and cut the antenna slots, and finally attach the dipoles antennas, results in relatively fixed absolute errors.

It is assessed that the main factors contributing to DF estimation error arises from the combined demodulator errors and antenna spacing errors. In terms of percentage, these errors increase as we reduce the distance between antenna elements. A higher percentage error decreases the accuracy of the DF system and increases the number of gross errors. For a RSNS-DF system with a shorter baseline, errors in phase differentials would have a greater impact, if the desired resolution is maintained.

G. LIMITATIONS AND CHALLENGES OF APPLYING VIRTUAL SPACING

From the simulations, it may seem that we can achieve ‘super resolution’ by applying the virtual spacing concept and increasingly larger virtual moduli sets. The simulation results in Figures 45 to 47 were conducted in ideal circumstances and do not address important practical issues such as noise and accuracy of antenna element spacing. Some of the key considerations, limitations and challenges of applying virtual spacing algorithm include:

1. Scaling Factor and Resulting FOV.

Depending on the original moduli set used, the scaling factor may increase or decrease the FOV. A high resolution over a very small FOV may not meet the needs of practical DF systems.

2. SNR to Support Error Free Coding.

A relatively high SNR of 30 dB was determined to provide a reasonable probability in correct bin estimation in [7]. The effects of SNR have yet to be determined for N -channel systems. It is likely that higher levels of SNR would be required as we increase resolution by using higher valued moduli sets, whilst maintaining the same probability of correct bin estimation.

3. Coding Errors and the Probability of Correct Bin Estimation.

This is related to the percentage phase differential error. RSNS coding errors are largely a result of system noise, phase differential errors from antenna element spacing and the centering of demodulator phase response. These errors ‘propagate downstream’ to the new virtual spacing magnified, as the estimated AOA's are determined from a single source of stream of I and Q data obtained from one set of antennas; i.e. the real spacing. The percentage phase differential error increases with shorter baselines, resulting in a lower probability of correct bin estimation.

Similar studies in achieving super resolution for imagery have yielded similar results for simulations [20]. Under a noise free environment, imaging resolution beyond classical diffraction limits is possible by bandwidth extrapolation and analytic continuation. Extrapolation methods for imaging systems have proved to be extremely sensitive to noise.

Although both imagery and DF systems deal with the nature of waves, RF signals are several orders of magnitude lower in terms of frequency and wavelength. Further investigation regarding coding errors on virtual spacing due to noise, antenna spacing error and demodulator response would need to be conducted to enhance our understanding on the practical limits on the level of resolution that is achievable for given SNR and phase errors in a DF system.

H. SUMMARY AND ANALYSIS OF DF PERFORMANCE

The overall DF performance for the first array using the moduli set {7 15 29} is remarkable, considering that the entire DF system was built entirely from COTS and the antenna elements were mounted by hand.

Since the same hardware is used for testing the two arrays, both the arrays suffer from the same set of error sources. These errors include the demodulator I/Q centering error, demodulator rotational error, noise in the electronics, antenna spacing errors, reflections from the walls of the anechoic chamber and approximating the spherical wave as a plane wave. As discussed in the previous section, these errors generally have a higher adverse impact on arrays with shorter baselines.

On hindsight, a longer baseline might have provided a more satisfactory set of results for the second array. The results obtained for the virtual spacing has similar shape and characteristics as the results obtained for the real spacing. However, virtual spacing results differ significantly from what was expected from the simulations, albeit the simulations were generally conducted in LabView for a noise free environment.

VIII. CONCLUSIONS AND RECOMMENDATIONS

The RSNS-based DF system shows tremendous promise and offers exciting possibilities for both commercial and military applications. Integrating the DF system with opportunistic phased array and aperstructure system, where transmit/receive modules are placed at available locations covering the whole superstructure and hull of a naval vessel, provides a large-scaled antenna configuration with an additional capability of direction finding.

High value surveillance aircraft like Rivet Joint, Cobra Ball and Joint Stars are not used to detect and DF Low Probability of Intercept (LPI) emitters. Detection of LPI radars, which transmit CW power in the milli-watt range, can only be achieved at short ranges. Placing the high value surveillance aircraft in close proximity of the emitter exposes them to unacceptable risks of being attacked. The RSNS-based DF system, with its small baseline requirements and light payload, can be integrated into UAV sensor suites. These UAVs can act as stand-in sensors to bridge the gap in surveillance capability for detection and DF of LPI emitters.

The application of the RSNS algorithm for direction finding is an ongoing project. With the digital architecture for the demonstration array fully implemented and functional, the next steps in bringing the RSNS-based DF system into a practical standalone system for real-world applications can be undertaken.

To further the progress made on the RSNS-based DF system, a number of focus areas needs to be examined with simulations and tests conducted.

A. SENSITIVITY ANALYSIS

A number of known error sources have been discussed in the thesis. To further our understanding on the adverse impact of these errors, sensitivity analysis on errors of interest should be conducted. Techniques such as Monte Carlo simulation on noise and demodulator phase error would enhance our

understanding of the system robustness. Simulations should also be extended to determine system response outside of the design frequency and the errors caused by the plane wave approximation.

B. REDUCING MAIN ERROR SOURCES

With the sensitivity analysis completed, efforts can focus on minimizing the main error sources.

1. Demodulator Board

The set of calibration data for I/Q offset used for this project has been verified over several iterations. However, the offsets were determined using a simple averaging of I and Q voltages. More sophisticated optimization techniques can be used to determine the true center of the demodulator response. Raw I and Q data from tests in the anechoic chamber can be saved for post-processing and different I and Q offsets tested to determine if the offsets can be optimized to reduce errors. Sourcing for alternative demodulator boards could also be considered if budget allows. Same here

2. Antenna Spacing

It is challenging to achieve the exact antenna spacing required. Besides the spacing, the vertical alignment and the distance at which antennas protrude from the ground plane also requires careful adjustment for uniformity. Even if precision milling for the ground plane is available, the antenna elements are still mounted by hand. While crude, careful measurements and alignment using foam or paper strips is the likely solution for the demonstration array in the short term. And here

3. Plane Wave Approximation

Corrections for the Hygen-Fresnel quadratic term were not incorporated into the current algorithm as applying the corrections are challenging when the reference antenna is not at the center of rotation. For future tests, the reference antenna should be centered to the pedestal rotational axis and aligned with the transmit antenna. This can be achieved by mounting an extension board onto the pedestal in the anechoic chamber. Corrections for the quadratic term should be applied, especially when using an array with a relatively long baseline.

C. OTHER PERMUTATIONS FOR VIRTUAL SPACING

The solution offered in this thesis for the virtual spacing of N -channels is one of many possibilities. Three specific areas should be studied:

1. Combination of Real Spacing for Virtual Spacing

Large permutations on combining real spacing to obtain the virtual spacing is possible, especially when large number of channels are used. The maximum achievable virtual spacing baseline would be the combination of all the real baselines, and the minimum virtual spacing baseline for non-PRP linear moduli is determined by subtracting all real baselines from the longest real baseline. Only three cases for virtual spacing have been determined in this thesis. The remaining equations for determining the virtual spacing of a three-channel system should be worked out and subsequently extended for N -channels.

2. Optimizing the Choice of Virtual Spacing Used

Rules of thumb for optimizing the sets of virtual spacing used are not available. Intuitively, it would seem combinations of real spacing that provide longer baselines for all the channels of the virtual antenna array would provide a lower probability of errors. Simulations in MATLAB should first be conducted for sensitivity analysis to known error sources. These simulations can be conducted for all permutations available for a 3-channel system to understand the

robustness against error sources. Lab tests with different combinations of virtual spacing should then be conducted to verify the simulation results.

3. Virtual Spacing for PRP Moduli Sets

The use of PRP moduli sets results in larger dynamic range and higher resolution. Studies to solve for applying the virtual spacing concept for PRP moduli sets should continue.

D. EXTENSION OF DEMONSTRATION ARRAY FOR WIDEBAND APPLICATIONS

In military naval applications, the ability for the wideband interception of RF signals from 2 to 18 GHz is required to encompass the range of threats faced by a naval platform. To extend the demonstration for wideband operations, a 2 to 18 GHz converter could be added prior to the LNA to down convert signals to the system operating frequency of 2.4 GHz. When the frequency is determined, usually through an instantaneous frequency measurement sub-system, the folding waveform changes can be predicted. The prediction of the change in folding waveforms can then be used to adjust the digital thresholds and subsequently for the resolving the signal AOA.

LIST OF REFERENCES

- [1] Lipsky, Stephen E. , *Microwave Passive Direction Finding*, pp 8-9, 155-164, John Wiley & Sons, New York, 1987.
- [2] Hendon H. Jenkins, *Small-Aperture Radio-Direction Finding*, pp 11-18, 61, Artech House, Norwood, Massachusetts, 1991.
- [3] Wickersham D., "Application of the Robust Symmetrical Number System to High Resolution Direction Finding Interferometry," Master's Thesis, Naval Postgraduate School, Monterey, California, 2000.
- [4] York N., "Design of a Phase Sampled Interferometry Antenna Using the Robust Symmetrical Number System," Master's Thesis, Naval Postgraduate School, Monterey, California, 2000.
- [5] Babb C.F., "Mixed Signal Processor for a Robust Symmetrical Number System Direction Finding Antenna," Master's Thesis, Naval Postgraduate School, Monterey, California, 2000.
- [6] Eng, C. S., "Digital antenna architectures using commercial off the shelf hardware," Master's Thesis, Naval Postgraduate School, Monterey, California, December 2003.
- [7] Chen J.C., "A Virtual RSNS Direction Finding Antenna System," Master's Thesis, Naval Postgraduate School, Monterey, California, December 2004.
- [8] Luke L. Brian and Pace P. E., "N-Channel RSNS Redundancy Analysis", Proceedings of the 2006 IEEE International Symposium on Information Theory. IT06 -1373, Seattle, WA, July 2006.
- [9] Styer D., Pace P. E. and Akin I. A., "A folding ADC preprocessing architecture employing a robust symmetrical number system with Gray-code properties," *IEEE Trans. on Circuits and Systems-II : Analog and Digital Signal Processing*, Vol. 47, No. 5, pp. 462–467, 2000.
- [10] Luke L. Brian, "Architecture of an Integrated Microelectronic Warfare System on a Chip and Design of Key Components", PhD Dissertation, Naval Postgraduate School, Monterey, California, 2004.
- [11] Styer D. and Pace P.E., "Two-channel RSNS Dynamic Range", *IEEE Transactions on Circuits and Systems - I : Fundamental Theory and Applications*, Vol 49, No.3,

- [12] Pace P. E., Wickersham D., Jenn D., and York N., "High Resolution Phase Sampled Interferometry Using Symmetrical Number Systems," *IEEE Transactions on Antennas and Propagation*, Vol 49, No. 10, pp. 1411-1423, 2001.
- [13] Burgstaller, G., "Wirelessly Networked Digital Phased Array: Design and Analysis of a 2.4GHz Demonstrator," Master's Thesis, Naval Postgraduate School, Monterey, California, September 2006.
- [14] Gezer, B. L., "Multi-beam Digital Antenna for Radar, Communications, and UAV Tracking Based on Off-the-Shelf Wireless Technologies," Master's Thesis, Naval Postgraduate School, Monterey, California, September 2006.
- [15] RF Bay, Inc. (rfbayinc.com), Data Sheet, "LNA-2700," <http://rfbayinc.com/LNA/LNA-2700.pdf>, last retrieved in July 2006.
- [16] Analog Devices (analog.com), Data Sheet, "AD8347 0.8 GHz to 2.7 GHz Direct Conversion Quadrature Demodulator," http://www.analog.com/UploadedFiles/Data_Sheets/230407246AD8347_a.pdf, last retrieved in July 2006.
- [17] National Instruments (ni.com), Data Sheet, "CompactRIO – Real-Time Embedded Controllers, NI cRIO-900x," http://www.ni.com/pdf/products/us/6358_crio_rt_controllers.pdf, last retrieved in August 2006.
- [18] National Instruments (ni.com), Data Sheet, "CompactRIO Reconfigurable Chassis, NI cRIO-910x," http://www.ni.com/pdf/products/us/cat_crio_9104.pdf, last retrieved in August 2006.
- [19] National Instruments (ni.com), Data Sheet, "C Series Analog Input Modules, NI-921x," http://www.ni.com/pdf/products/us/c_series_ai.pdf, last retrieved in August 2006.
- [20] Goodman W. Joseph, *Introduction to Fourier Optics*, pp 160-165, McGraw Hill, 1996

INITIAL DISTRIBUTION LIST

1. Defense Technical Information Center
Ft. Belvoir, Virginia
2. Dudley Knox Library
Naval Postgraduate School
Monterey, California
3. Chairman, Code PH
Naval Postgraduate School
Monterey, California
4. Prof. Phillip E. Pace
Department of Electrical & Computer Engineering
Naval Postgraduate School
Monterey, California
5. Prof. David C. Jenn
Department of Electrical & Computer Engineering
Naval Postgraduate School
Monterey, California
6. Prof. Donald L. Walters
Department of Physics
Naval Postgraduate School
Monterey, California
7. Prof. Micheal E. Melich
Meyer Institute
Naval Postgraduate School
Monterey, California
8. Prof. Rodney W. Johnson
Meyer Institute
Naval Postgraduate School
Monterey, California
9. Prof. William A. Solitario
Meyer Institute
Naval Postgraduate School
Monterey, California

10. Prof. Yeo Tat Soon
Director, Temasek Defence Systems Institute (TDSI)
National University of Singapore
Singapore
11. Robert D. Broadston
Department of Electrical & Computer Engineering
Naval Postgraduate School
Monterey, California
12. Mr. Steven Russell
Office of Naval Research
Arlington, Virginia
13. Dr Peter Craig
Office of Naval Research
Arlington, Virginia
14. Dr Frank Klemm
Office of Naval Research
Arlington, Virginia
15. Mr Alfred Di Mattesa
Office of Naval Research
Arlington, Virginia
16. Dr. Brian Luke
NIOC, Suitland
Suitland, Maryland
17. Mr. Bill Bigas
EDO Corporation
Morgan Hill, California
18. Mr. Dave Ford
EDO Corporation
Morgan Hill, California
19. Dr. Greg Donaldson
EDO Corporation
Morgan Hill, California
20. Dr. Don Newsome
EDO Corporation
Morgan Hill, California

21. Mr. Paul Eyring
EDO Corporation
Bohemia, New York